Atmospheric rivers drive exceptional Saharan dust transport towards Europe

Diana Francis [a,*], Ricardo Fonseca [a], Narendra Nelli [a], Deniz Bozkurt [b,f], Ghislain Picard [c], Bin Guan [d,e]

[a] Environmental and Geophysical Sciences (ENGEOS) Lab, Khalifa University, P.O. Box 127788, Abu Dhabi, United Arab Emirates
[b] Department of Meteorology, Universidad de Valparaíso, 2340000 Valparaíso, Chile
[c] University Grenoble Alpes, CNRS, Institut des Géosciences de l'Environnement (IGE), UMR 5001, 38041 Grenoble, France
[d] Joint Institute for Regional Earth System Science and Engineering, University of California, Los Angeles, CA, USA
[e] Jet Propulsion Laboratory, California Institute of Technology, Pasadena, CA 91109, USA
[f] Center for Climate and Resilience Research (CR)2, Santiago 8320000, Chile

ABSTRACT

This study highlights the occurrence of atmospheric rivers (ARs) over northwest Africa towards Europe, which were accompanied by intense episodes of Saharan dust transport all the way to Scandinavia, in the winter season. Using a combination of observational and reanalysis data, we investigate two extreme dusty AR events in February 2021 and assess their impact on snow melt in the Alps. The warm, moist, and dusty air mass (spatially-averaged 2-meter temperature and water vapour mixing ratio anomalies of up to 8 K and 3 g kg^{-1}, and aerosol optical depths and dust loadings of up to 0.85 and 11 g m^{-2}, respectively) led to a 50% and 40% decrease in snow depth and surface albedo, respectively, in less than one month during the winter season. ARs over northwest Africa show increasing trends over the past 4 decades, with 78% of AR events associated with severe dust episodes over Europe.

1. Introduction

Atmospheric rivers (ARs) are elongated and narrow bands of clouds and high water vapour content (Zhu and Newell, 1994), which advect low-latitude air poleward (Gimeno et al., 2014). ARs are believed to account for most of the annual moisture transport from the tropics into mid and high latitudes (e.g., Ralph et al., 2017). The poleward pathways of ARs are located mainly over oceans and their preferable landfall areas are over land. In this study, we identify for the first time the occurrence of ARs towards Europe via a new pathway: across the Sahara Desert, with the ARs originating in the eastern Atlantic Ocean.

When the tropical moisture stream within the ARs encounters topographical barriers, such as mountain ranges, it can lead to copious amounts of precipitation, triggering flooding and other hydrological extremes (e.g. Guan et al., 2016; Kingston et al., 2016; Waliser and Guan, 2017; Bozkurt et al., 2019; Dezfuli, 2020; Bozkurt et al., 2021; among many others). With an elevation of up to 4800 m and stretching over more than 1200 km, the Alps are the most prominent mountain range in Europe. Due to the combination of high latitude (~45°N) and

elevation, this region features several glaciers, with the snow cover being permanent above about 3000 m (Theurillat and Guisan, 2001). However, over the last 40 years there has been a pronounced reduction in the snow depth, in particular in regions below 2000 m where the snow cover is seasonal: it dropped at a rate of roughly 8% per decade, with the seasonal snow cover duration decreasing at about 6% per decade (Matiu et al., 2021). Snow plays a crucial role in the local economic (Rixen et al., 2011) and energy generation (Anghileri et al., 2018) activities. Moreover, the length of the snow season is more sensitive to climate change here compared to remote regions of North America and Eurasia (Evan and Eisenman, 2021). Hence, it is vital to understand the mechanisms responsible for the observed decrease in snow cover, both at local and synoptic-scales.

One process that can lead to a reduction in snow cover is the advection of warm and moist air, which can be pronounced if in association with episodic extreme weather events such as ARs. The impact of ARs on the melting of snow is nicely illustrated in Bozkurt et al. (2021) for the snowmelt season in the Taurus and Zagros mountains in the northern half of the Middle East. They found AR days to be wetter and

warmer than the all-day climatology, with precipitation and surface temperature anomalies of up to 2 mm day^{-1} and 1.5 °C, respectively, leading to an up to 30% decrease in the snowpack depth in the Zagros mountains (the effects on the snow at Taurus Mountains is elevation-dependent). Similarly, Little et al. (2019) reported on the role of ARs in the ablation of glaciers in the Southern Alps in New Zealand. In these melt events, in addition to sensible heat flux associated with the warmer temperatures, the increase in the downward long-wave radiation flux due to the presence of clouds and water vapour also contributes to the warming of the surface (Hegyu and Taylor, 2018; Wille et al., 2019).

Besides warm and moist air advection, aerosols, in particular mineral dust, can also lead to the melting of the ice and snow: when deposited on them, they darken the surface and lower its albedo (e.g. Tedesco et al., 2016), which leads to the absorption of a larger fraction of the incoming solar radiation and hence to a rise in the surface temperature and snowmelt (e.g. Stibal et al., 2017). In fact, Painter et al. (2018) showed that dust may play a bigger role in snowmelt (via shortwave absorption enhancement) compared to air temperatures (via sensible heat). Dumont et al. (2020) estimated that a single Saharan dust event in March 2018 may have shortened the snow cover duration in the Caucasus Mountains by up to 30 days, with a more pronounced effect at higher elevations. The daily-averaged surface radiative effect due to dust peaked at about 35 W m^{-2}, stressing its major contribution to the surface energy budget. Instantaneous values can be even larger, reaching up to 153 W m^{-2} for a site in the Alps (Di Mauro et al., 2015), where the snow-albedo feedback in response to Saharan dust can lead to the melting of the snow up to 38 days earlier than normal (Di Mauro et al., 2019). Mineral dust deposition on snow and ice can also impact further the life cycle of snow by favoring the development of microalgae. In fact, mineral dust aerosols can provide nutriments to the microalgae that grow on snow and ice and form the known cryoconite on Greenland Icesheet for instance (e.g., Nagatsuka et al., 2014).

Dust aerosols can be advected even further poleward by the warm conveyor belt associated with extratropical cyclones and ARs: e.g. Francis et al. (2018; 2019a) report on the role of Saharan dust aerosols in the Greenland ice melt, noting that the combined effect of the dust radiative forcing and the warm and moist air led to a 10 °C increase in the surface temperature for more than three consecutive days. While water vapour is known to be a major greenhouse gas in the atmosphere, dust has an anti-greenhouse effect in the visible and ultraviolet wavelengths but a greenhouse effect in the infrared and ultraviolet parts of the spectrum as it absorbs over a wide range of radiation wavelengths (Colaprete and Toon, 2003; Francis et al., 2021).

The two processes listed above, ARs and dust, are strongly intertwined. On the one hand, airborne dust can enhance the radiative effects of the water vapour, as the warming of the dust layer means the air can hold higher amounts of moisture, besides the fact that dust particles can act as cloud condensation nuclei, promoting the development of clouds (Karydis et al., 2011; Francis et al., 2020a). On the other hand, ARs typically occur in regions of large pressure gradients, with a cyclone to the west and a ridge to its east and south (in the northern hemisphere), leading to strong near-surface winds (Shinoda et al., 2019). The high-speed near-surface winds can lift dust from the surface if the AR goes through a desert region such as the Sahara (e.g. Bozkurt et al., 2021). In fact, several authors have noted the advection of dust from the Sahara into Europe primarily in the warm sector of extra-tropical cyclones (e.g. Bou Karam et al., 2010; Fiedler et al., 2014, 2018, 2019; Kaskaoutis et al., 2019), although it can also occur in the cold sector (Voss, 2020).

As in the middle of winter snow is typically extensive in the mountainous region, and given that dust is known to reduce the surface albedo and increase its temperature (Tedesco et al., 2016; Stibal et al., 2017), the dusty ARs are bound to have an impact on the snow cover. What is more, when combined with the presence of abundant moisture, such as in association with an AR, the increase in the downward longwave radiation flux may exacerbate the depletion of snow (e.g., Francis et al., 2020b). Recent studies have indicated a tendency for an increase in the

number of ARs in the region in a warmer climate (Massoud et al., 2020; Payne et al., 2020), which may pick up dust as they travel across the Sahara, stressing the need to better understand the genesis and effects of such events.

Previous studies focused separately on the radiative effects of airborne dust (e.g. Helmert et al., 2007; Kaskaoutis et al., 2019) and on the impact of water vapour (e.g. Wille et al., 2019; Davolio et al., 2020; Francis et al., 2020b) over certain regions, but the combined effect of the two, as is the case during dusty AR events, has been overlooked. This is achieved in this work for two dusty ARs that affected the Alps in February 2021, triggering an exceptional darkening and subsequent melting of snow in the middle of a winter season, with potential implications for the local economic activities. The two dusty ARs can be seen in the visible satellite images of Figs. 1A-B, with their effect on the snow cover (i.e. darkening) highlighted when the snow cover on 26 January 2021 (Fig. 1C) is compared with that on 07 March 2021 (Fig. 1D).

The main objectives of this work are (i) to highlight the presence of dusty ARs over Europe and analyze the meteorological conditions favoring their occurrence; (ii) to assess the impact of both ARs and dust on snow melt at the Alpine Mountain range where, due to the interaction of the flow with orography, ARs can make landfall and dust is deposited. To this end, we investigate the extreme dust events which occurred in Europe in February 2021. To provide a historical context for these events, a climatology of ARs and dust event occurrence during the period Jan-May 1980–2017 is also presented. This paper is structured as follows. First, the synoptic-scale atmospheric state that accompanied the selected AR cases is discussed, followed by the analysis and quantification of the associated poleward transport of water vapour and dust. The radiative forcing is then estimated both using in-situ measurements at a weather station in the Alps, and satellite- and model-derived products for a larger-scale perspective. Finally, as these events may become more frequent in a warmer world (e.g. Espinoza et al., 2018; Massoud et al., 2020; Payne et al., 2020), the climatology and trends in ARs and dust storms over Europe is presented. The main findings of the work are outlined in the "Summary and Conclusions" section, while in the "Materials and methods" section, the observational and modelled datasets employed as well as the methodology followed in the analysis are described.

2. Results and discussion

2.1. Synoptic conditions for Atmospheric rivers occurrence over the Sahara and Europe

Two dusty ARs affected the Alps during February 2021: one at the beginning of the month from 04 to 09 (Fig. 1A), and another from 18 to 25 (Fig. 1B). In both satellite images, the plume of dust from the Sahara Desert into Europe, shaded in brown, can be seen (on the second event it extended all the way to Denmark and southern Sweden). Fig. 2 summarizes the associated synoptic conditions.

On 05 February (Fig. 2A) a wavy polar jet was present, with a trough over the Iberian Peninsula and a ridge over Italy and Greece. The resulting pressure gradient (Fig. 2C) gave rise to southerly winds, which advected the warm and more moist tropical Atlantic air over the Sahara desert and into Europe. The air mass likely picked up moisture as it travelled over the Mediterranean Sea, as was the case in other AR events (e.g. Davolio et al., 2020). The pressure dipole shifted eastwards in the following days (Fig. 2C) and dissipated over Eastern Europe around 11 February. Snow started to fall in the Alps on 07 February (fig. S1, A–C), as the low over Spain and the associated cold front pushed eastwards into Central Europe.

The large-scale circulation during the second event (Fig. 2B) featured an omega blocking, with a ridge over central Europe and a trough to its west and east, the former much deeper than the latter and extending into northwestern Africa. The trough over northwestern Africa eventually developed into a cut-off low over Algeria and Tunisia (Fig. 2A, fig. S2, A
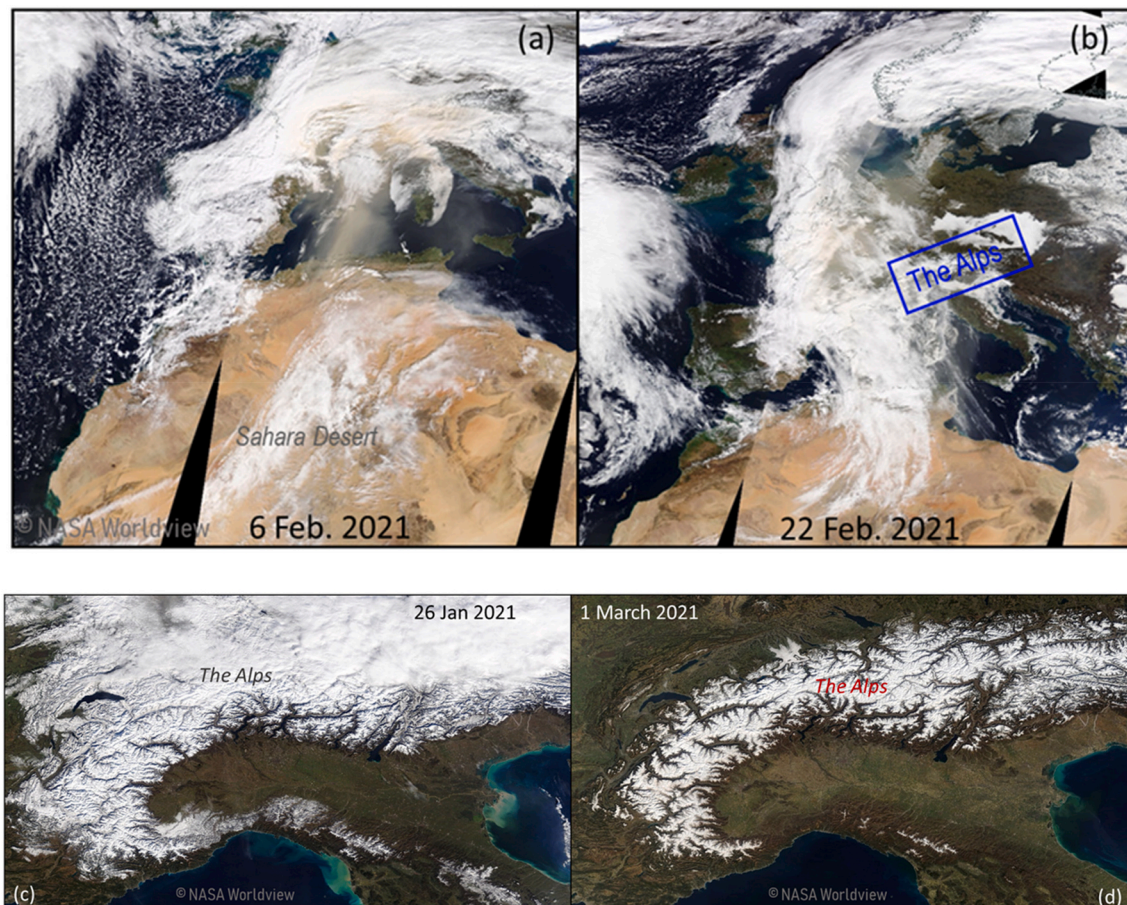
Fig. 1. The dusty Atmospheric Rivers (ARs) of February 2021. MODIS visible image on (a) 06 and and (b) 22 Feb 2021 over Northern Africa and Europe. Clouds are shown in white while dust is given in brown. The impact of the dusty ARs on the snow cover in the Alps can be seen by comparing the MODIS visible images on (c) 26 January 2021 and (d) 01 March 2021. (For interpretation of the references to colour in this figure legend, the reader is referred to the web version of this article.)

and B) with the southerly flow ahead of it promoting the advection of Saharan dust into Europe. As opposed to the first event, the pressure dipole in late February 2021 persisted for about 5 days (Fig. 2C) before the ridge tracked westwards and forced the low to move into the Atlantic Ocean. This synoptic pattern is consistent with the further poleward extension of the dust plume compared to the first event (Fig. 1, A and B). The normalised anomalies of the mid-tropospheric geopotential height (Fig. 2, A and B) and of the sea-level pressure (Fig. 2C) are up to two standard deviations away from the mean, which underscores the extreme nature of the two events. The near-surface fields (Fig. 2D) highlight the advection of tropical air from the Atlantic and equatorial Africa into Europe during the two AR events, which collected Sahara dust and moisture over the Mediterranean Sea along the way. The 2-meter temperature anomalies are up to three standard deviations away from the mean over parts of north Africa and west and central Europe, with the largest values aligned in a more southwest-northeast path on 05 February, while on 21 February they occurred in a more southerly-northerly direction, both consistent with the pressure patterns (Fig. 2, A–C).

Fig. 3 characterizes the two ARs in terms of the associated Integrated Vapour Transport (IVT; e.g., Ralph et al., 2019). Ahead of the trough over Western Europe on 06 February (Fig. 3A) the associated south-westerly flow brought moist air from the tropical Western Africa and its Atlantic coast into southern Europe, with a maximum IVT over northern Africa of 400–600 kg m^{-1} s^{-1}. This corresponds to a weak to moderate AR using the classification of Ralph et al. (2019), even though these IVT values are comparable to those estimated in the ARs that triggered the 10 largest floods in the Rhine catchment area in Germany from 1817 to

2015 (Ionita et al., 2020). In order to put this event in context, Fig. 3C gives the IVT and 500 hPa geopotential height anomalies at the same time, along with the major AR features. This AR event featured anomalies of up to 200 kg m^{-1} s^{-1} (or $^1/_3$ of the observed total value), which exceeded 1.5 standard deviations in a broad region extending from the tropical Atlantic at 15°N, to central Europe and the Alps at 45°N. Downstream of the ridge over the Black Sea and surrounding region, the IVT was in the range 150–300 kg m^{-1} s^{-1}, with moisture advection around the high clearly seen (Fig. 3, A and C). This AR had a predominant southwest-northeast orientation, extending over more than 5000 km, which is ~35% longer than the global average AR length of ~3700 km (Guan and Waliser, 2015).

In the second AR event, while the maximum IVT was comparable, the moisture plume reached all the way to northern Europe and Scandinavia at 60°N (Fig. 3B). The vast majority of the ARs in Europe in the cold season tend to occur between 45° and 55°N, mostly in association with a meridional pressure dipole over the Atlantic with a trough over Iceland extending into northern Europe and a ridge to its south, which corresponds to the positive phase of the North Atlantic Oscillation (Lavers and Villarini, 2013). However, Lavers and Villarini (2013) reported ARs up to 70°N, even though the driving large-scale circulation of these was primarily zonal and hence associated with limited amounts of dust, the opposite of that seen in this event. This is in line with the findings of Benedict et al. (2019), who noted that the ARs affecting Norway/western Scandinavia mostly originate from the central Atlantic Ocean. On 22 February the AR was directly connected to the lower latitudes (Fig. 3D) was associated with IVT anomalies over Europe exceeding 200 kg m^{-1} s^{-1}, and were also more than 1.5 standard deviations away from the

(a)

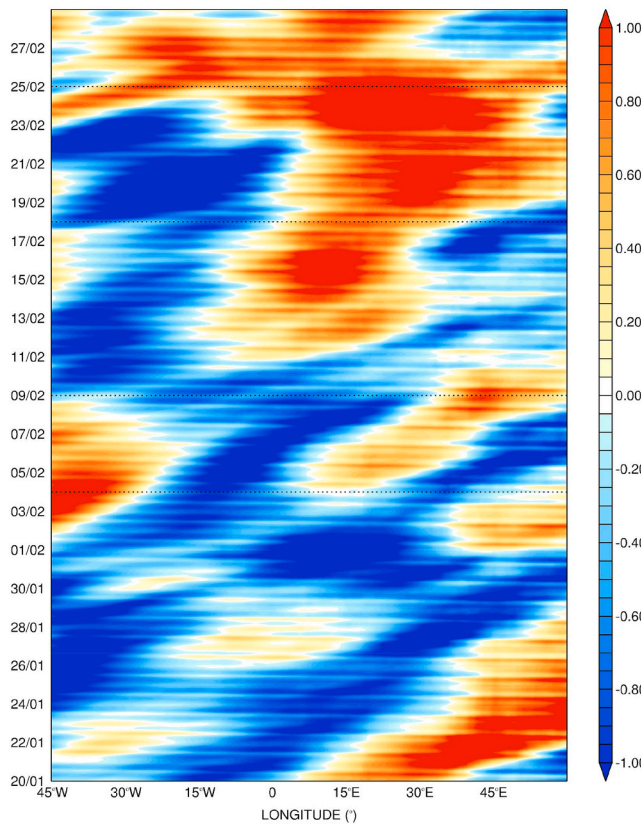### Z(500hPa) [m] & 200hPa WIND [ms^{-1}] ON 05-FEBRUARY-2021 @ 12UTC
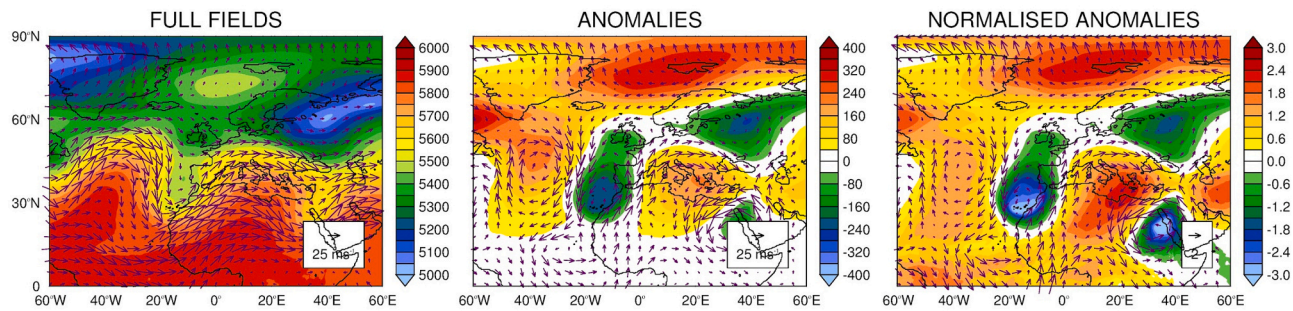
(b)

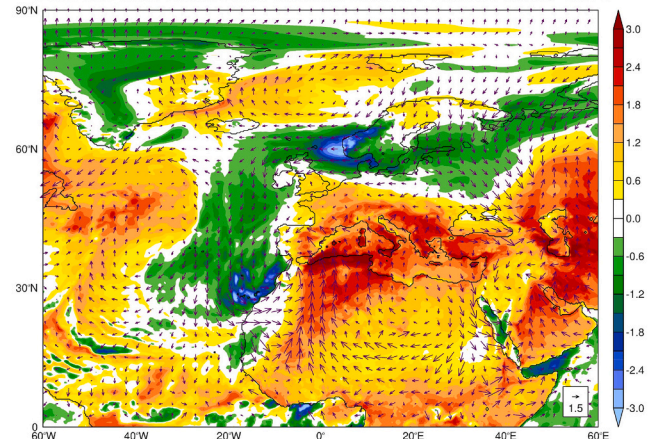### Z(500hPa) [m] & 200hPa WIND [ms^{-1}] ON 21-FEBRUARY-2021 @ 12UTC
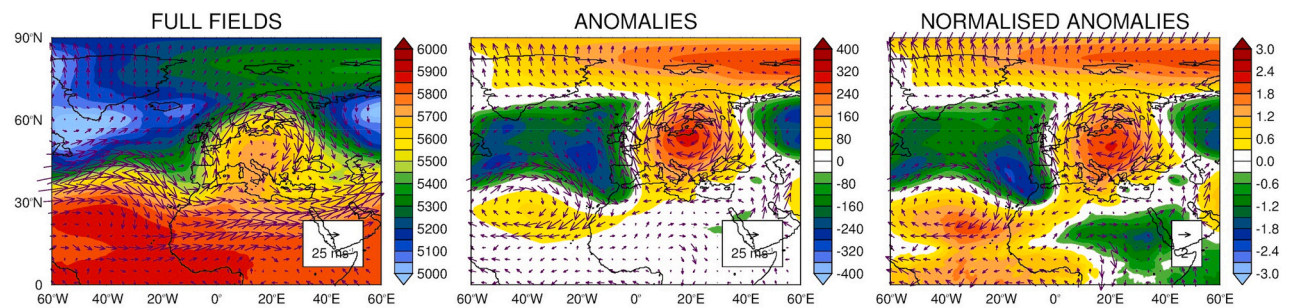
(c)

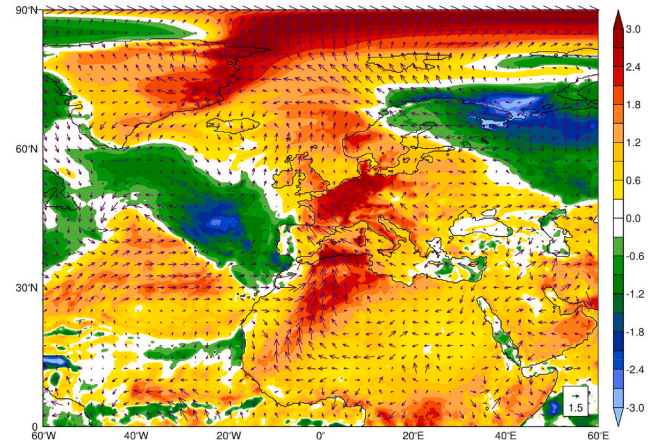SLP NORMALISED ANOMALIES AVERAGED OVER 20°N-60°N FOR 20 JAN - 28 FEB 2021

(d)

T2M & 10-M WIND NORMALISED ANOMALIES ON 05-FEBRUARY-2021 @ 12UTC

T2M & 10-M WIND NORMALISED ANOMALIES ON 21-FEBRUARY-2021 @ 12UTC

(caption on next page)

Fig. 2. Synoptic-scale circulation that favoured the poleward transport of dust and water vapour. (a) and (b) give the 500 hPa geopotential height (shading; m) and the 200 hPa horizontal wind vector (arrows; m s^{-1}) at 12 UTC on 05 and 21 February 2021, respectively, from ERA-5. Shown are the full fields, anomalies and normalised anomalies, the latter two with respect to the 1980–2020 ERA-5 climatology. In (c), the normalised daily mean sea-level pressure anomalies averaged over 20–60°N are plotted from 20 January to 28 February 2021, while (d) is as (a)-(b) but for the normalised 2-meter temperature and 10-meter horizontal wind vectors. The horizontal dashed lines in (c) represent the start and end dates of the dusty AR events.
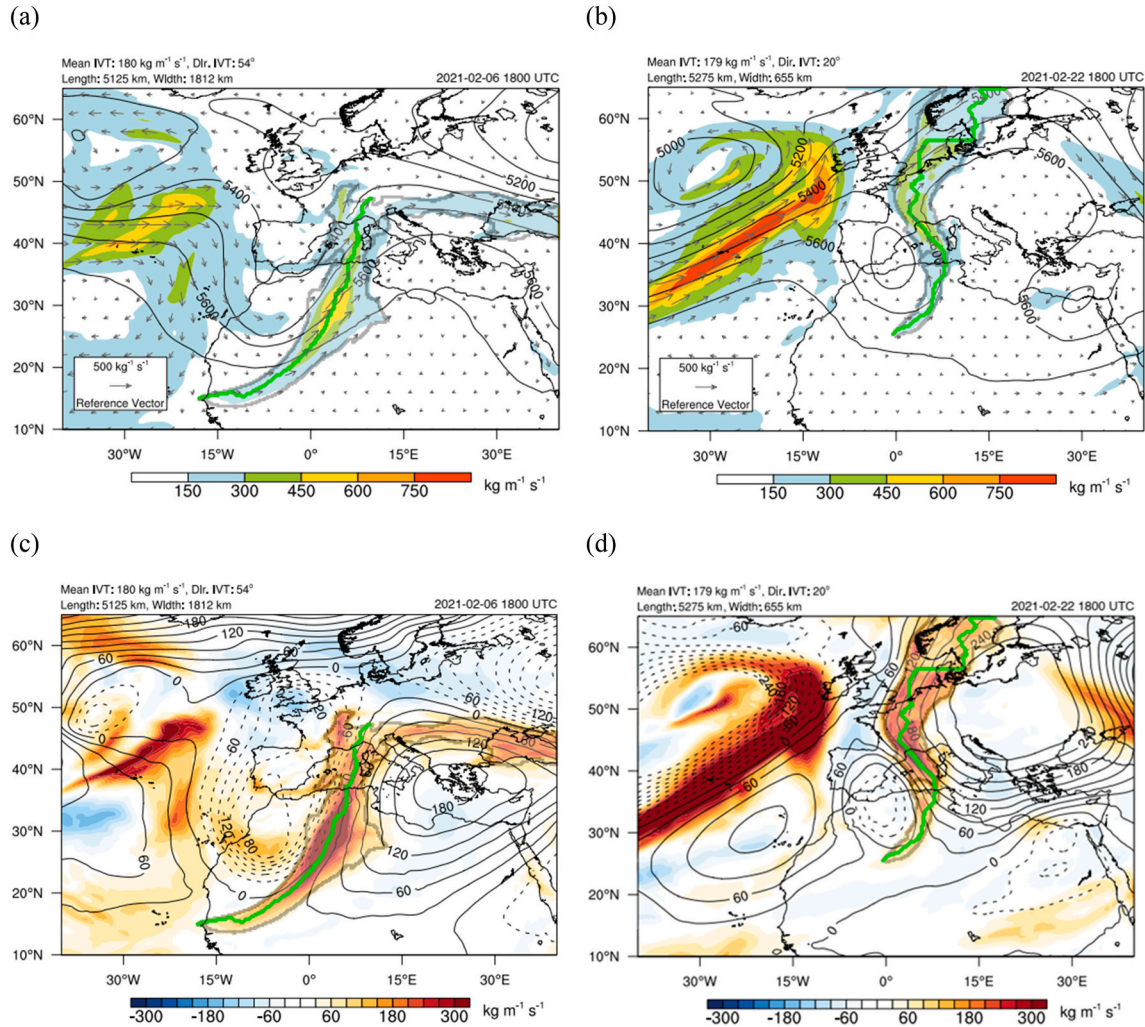

Fig. 3. AR occurrence and characteristics. (a) Integrated water vapour transport (IVT; kg m^{-1} s^{-1}) and 500 hPa geopotential height (Z500; m) on 06 February 2021 at 18 UTC. The shading denotes the magnitude of the IVT, with the arrows giving its eastward and northward components. The AR main features, such as the mean IVT, direction, length and width, are given at the top left of the plot. The light brown line denotes the AR shape, while the green line shows the AR axis. (b) is as (a) but on 22 February 2021 at 18 UTC. (c) IVT (shaded) and Z500 (contour lines) anomalies on 06 February 2021 at 18 UTC with respect to the 04–07 February climatology (1981–2010, 18 UTC) (d) is as (c) but for 22 February 2021 at 18 UTC with respect to the 20–23 February climatology (1981–2010, 18 UTC). (For interpretation of the references to colour in this figure legend, the reader is referred to the web version of this article.)

climatological values (not shown). What is more exceptional, this AR's geometry is more in line with the traditional definition of a narrow and elongated band of moisture being advected poleward, with a length and mean IVT comparable to those of the AR in early February, but with around a three times larger length-to-width ratio.

In summary, the two ARs discussed in this study were highly anomalous with respect to the climatological state. This is consistent with the results of Bozkurt et al. (2021) who highlighted that although African atmospheric rivers are largely weak due to travelling over the Sahara Desert, they can have significant impacts over the mountainous regions. The second event in particular extended all the way to northern Europe, in an unusual southerly-northerly direction, as opposed to the more common southwesterly-northeasterly orientation of the ARs in the region (Pasquier et al., 2019). In the next subsection, the poleward transport of dust and moisture that accompanied the ARs, as well as the

associated radiative forcing, are discussed.

2.2. Poleward transport of dust and water vapour and radiative forcing

Figs. 4 and 5 summarize the transport of dust and water vapour by the two ARs with Hovmoeller plots of longitude-averaged dust surface mass and optical depth, water vapour mixing ratio and temperature at 2-meters, IWV and surface net radiative flux and energy flux from 20 January to 28 February 2021. The vertical distribution of the dust can be inferred with the three-dimensional aerosol type profiles observed by the CALIPSO satellite (fig. S1, fig. S2).

In the two events, and for both the surface dust mass and optical depth, the normalised anomalies exceed two standard deviations away from the mean, reaching up to ~50°–55°N in the first event and going beyond 60°N in the second (Fig. 4, A and B). In the 40–50°N latitude
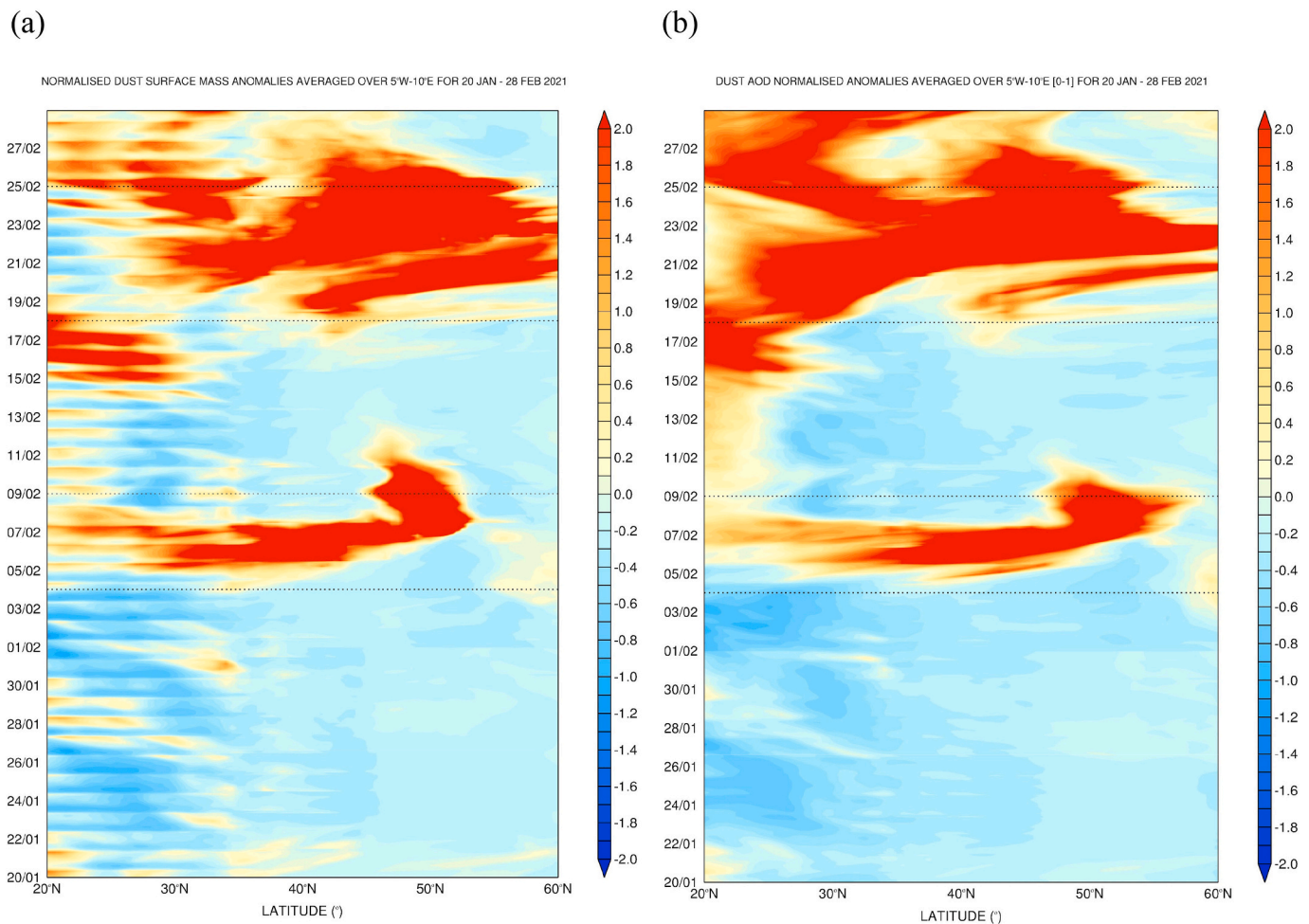
(a)

NORMALISED DUST SURFACE MASS ANOMALIES AVERAGED OVER 5°W-10°E FOR 20 JAN - 28 FEB 2021

(b)

DUST AOD NORMALISED ANOMALIES AVERAGED OVER 5°W-10°E [0-1] FOR 20 JAN - 28 FEB 2021

Fig. 4. Poleward transport of dust and water vapour. (a) and (b) show the normalised anomalies of dust surface mass and dust optical depth, respectively, averaged over 5°W-10°E and plotted from 0 to 60°N from 20 January to 28 February 2021 from MERRA-2. The anomalies are computed with respect to the 1980–2020 climatology. (c) gives the normalised integrated water vapour (IWV; kg m^{-2}) anomalies, averaged over 0°–10°E and plotted from 20 to 80°N for the same period from ERA-5, with the anomalies also with respect to the 1980–2020 climatology. In (d), the top panel shows the number of events of a given 550 nm dust optical depth for the 1980–2020 January–May period (red) and 1980–2020 February (blue) from MERRA-2, averaged over 43.5°–47.5°N and 5.5°–13.5°E. Each bin has a width of 0.1, with the midpoint labelled in the horizontal axis. AOD values less than 0.4 and in excess of 1.0 were excluded from the analysis. The observed dust optical depths from 20 January to 28 February 2021 are plotted below. (e) is as (d) but for the IWV from ERA-5. The range of values shown is 1 to 27 kg m^{-2}, in intervals of 2 kg m^{-2}. The horizontal dashed lines on all hovmoller plots represent the start and end dates of the dusty AR events. (For interpretation of the references to colour in this figure legend, the reader is referred to the web version of this article.)

band, the observed aerosol optical depth (AOD) values reached up to 0.30–0.35, with values of up to 0.2 at 60°N on 21–23 February (fig. S3A). While these AODs are unprecedented for the winter season (e.g. as noted by Israelevich et al. (2012), the AODs in the region are typically smaller than 0.1 for January and February, peaking in the spring and summer months), they can be observed in the warmer months (e.g. Barkan et al. (2005) reports AODs in excess of 2 for a dust event in July 1988). Hence, for the coldest months of the year, the observed dust AODs in the 40–50°N latitude band were unusual, in line with the normalised anomalies (Fig. 4, A and B). This is further confirmed by the 1980–2020 climatological AODs for the months of February and January–May over the Alps, as well as that observed from 20 January to 28 February 2021 over the same area (Fig. 4D). The area-averaged AODs were in the order of ~0.85 on 07 February 2021 and ~0.45 on 21–24 February, clearly on the higher end of the climatological values (Fig. 4D). The daily accumulated dust column mass over Europe (30°–50°N, 15°W–15°E) reached 22 kg m^{-2}, or approximately 160 Tg, on 21 February 2021, roughly seven times larger than the 1980–2020 background values (not shown). The daily accumulated dust loadings

reach 60 g m^{-2} over parts of the Alps, which is up to one order of magnitude higher than those reported by Varga (2020) for selected wintertime dust events in southern Europe.

Furthermore, the poleward transport of dust was analyzed more in depth based on four selected CALIPSO overpasses, two for each event (fig. S1, D and E, fig. S2, C and D). The overpass on 06 February shows a gradual increase in the vertical extent of the tropospheric aerosol from 25°N (~2 km) to 50°N (~7 km), as it is transported by the warm conveyor belt ahead of the surface cold front (fig. S1, A and D). An inspection of the aerosol subtype revealed it is predominantly dust, with a small contribution of polluted dust, a mixture of dust with biomass burning and urban pollution (Kim et al., 2018). The overpass on 07 February also shows dust aerosol up to 7 km high (fig. S1E), even though its signal is mostly masked by deep convective clouds that extend higher up in the atmosphere (fig. S1B). The overpasses on 21 and 23 February (Figs. S2c-d) also indicate the presence of dust aerosols up to 7 km high, even at 55–60°N in the overpass on 21 February. Saharan dust has been recorded above the Arctic Circle: e.g. Rodriguez et al. (2008) measured optical depths of up to 0.5 at an observatory in Svalbard at 79°N, in the

(c)

IWV NORMALISED ANOMALIES AVERAGED OVER 0°-10°E FOR 20 JAN - 28 FEB 2021
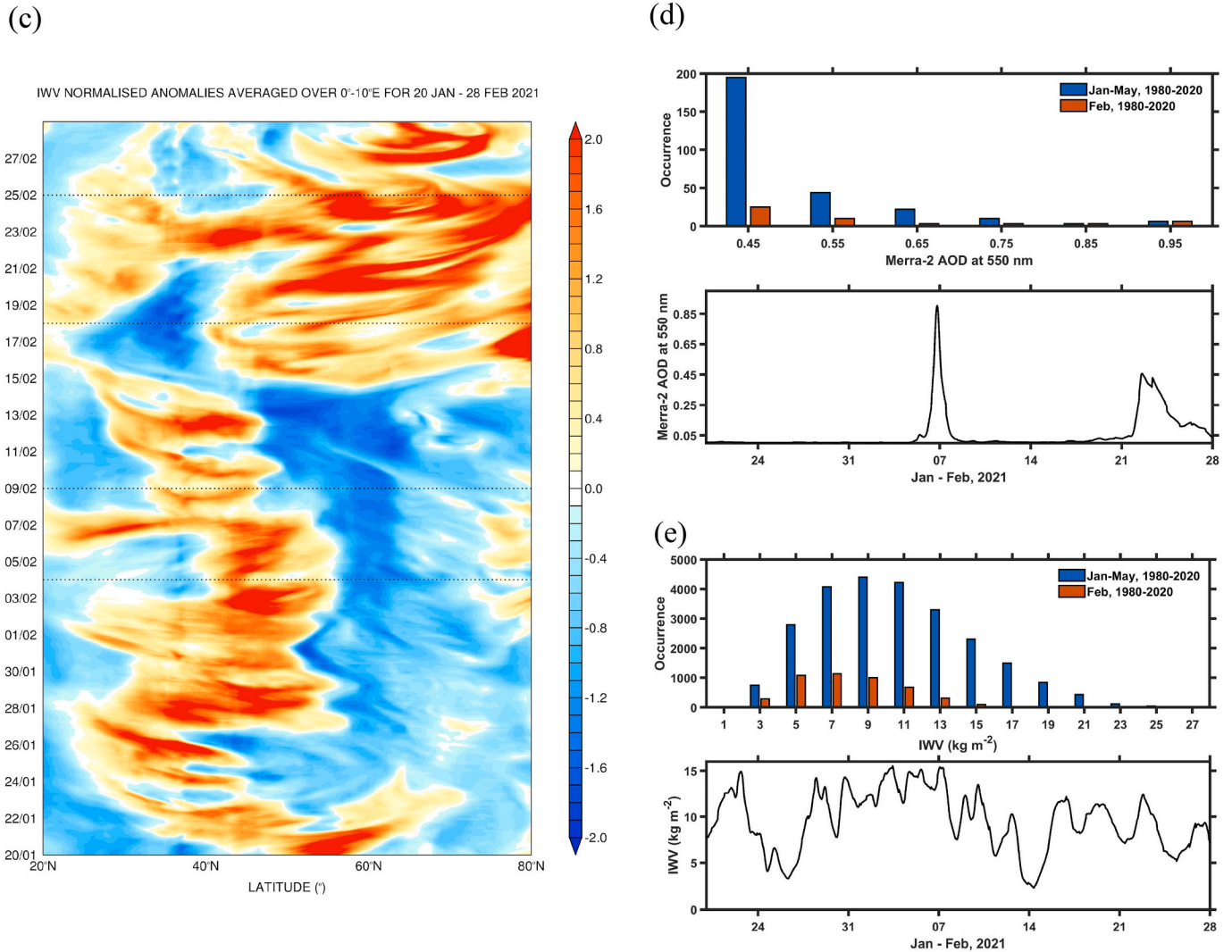

(d)

(e)

Fig. 4. (*continued*).

summer of 2006. However, such northward excursions occur almost exclusively in the spring and summer months (e.g. Barkan and Alpert, 2010; Francis et al., 2018) when a trough over Western Europe and northwestern Africa co-exists with an eastward displacement of the Icelandic low. The large-scale set-up in the second AR event with a persistent omega blocking over Europe (Figs. 2, B–D) and the time of the year when it took place, mid-winter (when the aerosols at higher latitudes are more confined to lower elevations; Thomas et al., 2019), makes the northward extent of the dust layer truly remarkable. Despite the presence of dust at altitudes as high as 7 km, when all the overpasses for February 2021 are considered, dust is found to be mostly confined to lower elevations around 1–3 km (fig. S4A) while the cloud profile shows a peak at lower elevations around ~2 km roughly where the dust amount is maximized, and another around 7 km. The latter is an indication of high-level clouds, some associated with deep convective clouds seen in the CALIPSO overpasses (fig. S1, D and E, and fig. S2, C and D). The advection of dust aerosols from lower latitudes into the Alps from 21 to 23 February (fig. S2, C and D), took place mostly along to slightly ahead of the AR (Fig. 3D). The same conclusion is reached when comparing the position of the AR with that of the dust layer during the first AR event (Fig. 3C, fig. S1, D and E) showing that the two are mostly in phase.

Fig. 4C shows the normalised IWV anomalies, which can be compared with the full values for the period 20 January to 28 February

2021 (fig. S3B). In line with the correspondent dust plots (Figs. 4a–b and Fig. S1e) during the second AR event the moist low-latitude air penetrated further poleward, with IWV values higher than 20 kg m^{-2} at 60°N and 10 kg m^{-2} at 80°N on 21 and 24 February (fig. 4S3b), both in excess of 2 standard deviations above the mean. Such values are typically only observed in the warmer months (Buehler et al., 2012), as the colder higher-latitude atmosphere cannot hold such high amounts of moisture. Their occurrence suggests the presence of warm and moist air (Fig. 5, A and B). As in the correspondent IWV plot (Fig. 4C) there is a broad swath of IWV values in excess of 1.5 standard deviations from roughly 40°N to 80°N from 18 to 25 February 2021. Air temperatures between 280 and 285 K and mixing ratios in the range 5–6 g kg^{-1} were ubiquitous in the region (not shown), which are up to 10 K and 2 g kg^{-1} above the 1980–2020 climatological background, respectively (Figs. S3c-d). In the Alps at about 50°N, the air temperature and mixing ratio anomalies were up to roughly 8 K and 3 g kg^{-1}, respectively (fig. S3, C and D), a comparable magnitude to that seen in the first AR event, which only reached around 50°N. As noted before, the area-averaged dust AOD over the Alps was anomalous for the month of February (Fig. 4D) with the same being true for the IWV values (Fig. 4E). In the 1980–2020 February climatology, the IWV in the region was generally below 10 kg m^{-2}, while in February 2021 values as high as 15 kg m^{-2} were observed, on the higher end of the climatological range. The slightly higher IWV values in the first event are consistent with the IWV Hovmoeller plots (Fig. 4C, fig.
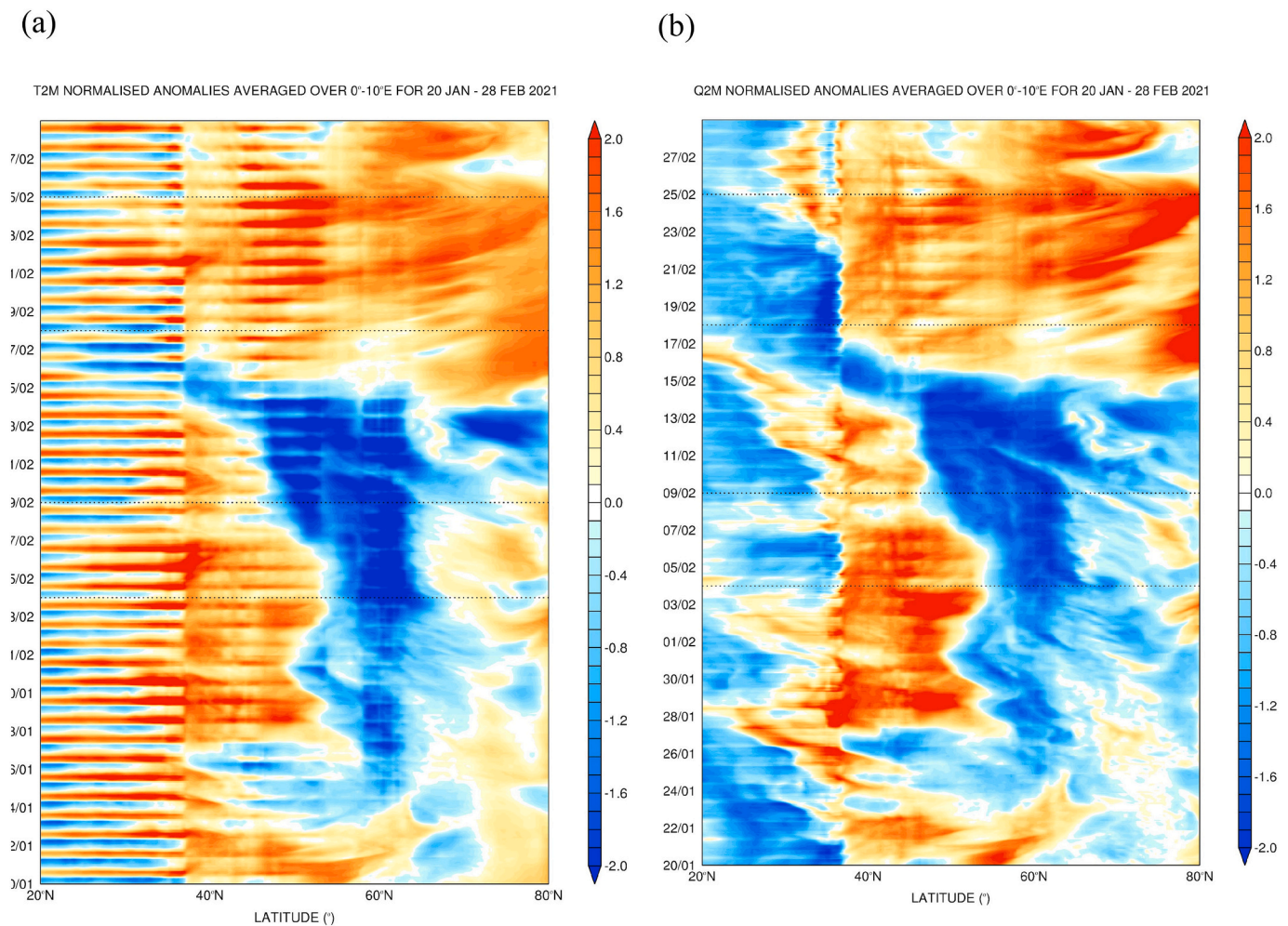
(a)   (b)

Fig. 5. Surface and atmospheric response to the ARs. Panels show the normalised anomalies averaged over 0–10°E of the 2-meter (a) temperature and (b) water vapour mixing ratio, and surface (c) net radiative flux (R_{net}) and (d) total energy flux (F_{net}) from 20 January to 28 February 2021 from ERA-5. The anomalies are computed using hourly data and with respect to the 1980–2020 climatology, and plotted from 20°N to 80°N. The horizontal dashed lines on all hovmoller plots represent the start and end dates of the dusty AR events.

S3B), and the synoptic-scale pattern (Fig. 2), which show that the second event affected regions mostly to the north of the Alps due to the presence of a blocking high over central and eastern Europe. Although higher IWV anomalies were observed during the second event (Fig. 4C), higher IWV actual values were observed during the first AR event (fig. S2B). This reflects the exceptional nature of the second event compared to the climatological mean at the latitudes reached by the AR and which were higher (drier atmosphere) than the latitudes reached by the AR during the first event.

The two ARs in February 2021 had levels of dust and moisture that were more typical of a spring season event (Fig. 4, D and E). The peaks in IWV and dust AOD are roughly in phase (Fig. 4, D and E). On the other hand, the cloud liquid water content in February 2021 was mostly within the climatological range (fig. S4B), without a clear phase shift with respect to the dust AOD (Fig. 4D) and IWV (Fig. 4E) time-series. The absence of clouds in the second event is consistent with the fact that the main AR axis was to the west of the Alps (Fig. 3, B and D), in line with the SEVIRI images (fig. S2, A and B), which show that the cut-off low to the south became detached from the cold front further north.

It is also of interest to assess the radiative impact of the ARs, in terms of the surface net radiation flux (R_{net}) and surface total energy flux (F_{net}) (Fig. 5, C and D, fig. S3, E and F). In these fields, positive values indicate fluxes away from the surface and negative values indicate energy input

towards the surface. The first AR event does not have a clear signature, in particular in R_{net}, while the second is clearly seen in both fields, with anomalies of up to 200–250 W m^{-2} and normalised anomalies mostly in the range 1–2. The fact the anomalies in F_{net} have a larger magnitude, stresses the important role of the surface heat fluxes in the response to the ARs, as F_{net} is given by R_{net} plus the contributions from the surface sensible and latent heat fluxes. This is not surprising, as at higher latitudes, and in the middle of the winter season, the downward shortwave radiation flux, which typically dominates R_{net}, is rather small. The magnitude changes in R_{net} and F_{net} reported here are comparable to those presented in Francis et al. (2020b), for two ARs in Antarctica at the end of the local winter season. Around the Alps, and in particular for the second event, the changes in the surface heat fluxes of roughly 100 W m^{-2}, as given by the difference between F_{net} and R_{net}, are also within the range of those estimated during AR events that affected the New Zealand Southern Alps in the summers of 2010–2012, which led to the extreme ablation of a local glacier (Little et al., 2019).

In the next subsection, the effects of the increased surface heating and subsequent snow melt in the Alps are discussed and put in context with other AR events.
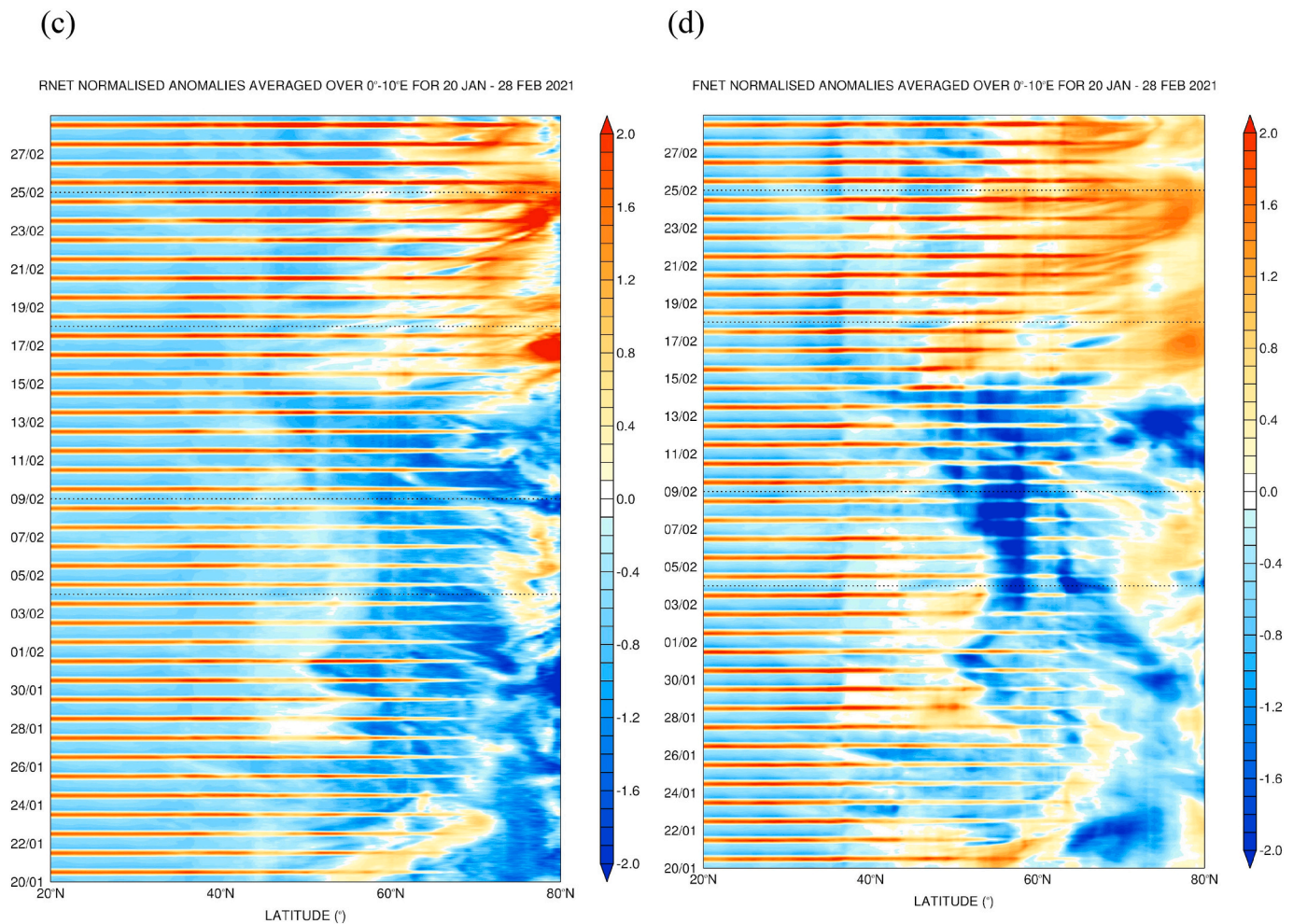
(c)

RNET NORMALISED ANOMALIES AVERAGED OVER 0°-10°E FOR 20 JAN - 28 FEB 2021

(d)

FNET NORMALISED ANOMALIES AVERAGED OVER 0°-10°E FOR 20 JAN - 28 FEB 2021

Fig. 5. (*continued*).

2.3. Impact of ARs and dust on albedo and snow melt

Over the Alps, the first AR event is seen during 06–07 February 2021 and the second on 21–23 February 2021 (Fig. 2C). One can see the intense dust occurrence during the same periods (Fig. 4D). In this section, we present the impact of the dusty ARs on the surface albedo and snow melt over the Alps, by analyzing surface radiation fluxes, albedo and snow depth from (i) in-situ measurements at a meteorological tower, (ii) satellite (CERES), (iii) ERA-5 reanalysis and (iv) GEOS-5 model-assimilated products.

The daily averaged surface net radiation flux (R_{net}) from CERES over 40.5°-49.5°N and 0°-15°E for 08 and 23 February (Fig. 6, A and B), show an increase in R_{net} over the Alps and surrounding region due to the moist and dusty air mass, with values exceeding 50 W m^{-2} in the second event. As estimated from the tower observations (Fig. 6C), due to the arrival of the AR, the air temperature increased by up to 10 K, the LW down increased by up to 50 W m^{-2}, and the surface albedo decreased by 40%. Note that the increase in LW down during the second AR event is only seen on 22 Feb 2021. This is due to the fact that the main AR axis is to the west of Alps (Fig. 3, B and D).

In terms of the area-averaged R_{net} and total energy flux (F_{net}) (Fig. 6, A, B–D), by and large R_{net} is below the climatological values during late January 2021, but increased during the month of February. With the occurrence of dusty ARs over the Alps, the area averaged F_{net} switched from negative (away from the surface) to positive (towards the surface) with a maximum of 6 W m^{-2} on 03 February and 12 W m^{-2} on 23 February. The sudden dip in F_{net} on 13 February was due to the passage

of a cold front over the Alps (not shown). At the tower location, the snow depth dropped by 0.76 m between 12 February and 11 March, corresponding to ~69% of the mean value (1.1 m).

For comparison, the seasonal melt of similar amount of Alpine snow requires a few months and is mostly due to wind-driven processes ranging from orographic precipitation at large scale to preferential-deposition of snowfall and wind-induced transport of snow on the ground at smaller scales. These processes play a key role in all the different stages of the evolution of seasonal snow in the Alps in addition to the gradual increase during summer in air temperature and the incoming solar radiation and turbulent and heat fluxes (Mott et al., 2018).

Regarding the spatial variability in GEOS-5 surface albedo and snow depth (Fig. 6, E-H), at the beginning of March, and with respect to early February, the albedo dropped by up to 40% and the snow depth by up to 50%. The snowfall associated with the first AR event, which made landfall over the Alps, helped to recover the surface albedo. However, the second AR event made landfall further north and west, and due to the dust deposition on the snow, the albedo decreased, with an overall reduction of 40%. The agreement between the tower and ERA-5 is excellent until the first deposit when the surface albedo (Rnet) started to decrease (increase) more rapidly in the observations than in the re-analysis. The meteorological tower being located on a south facing slope, dust rapidly emerged on the surface after the snowfall of Feb 8 while other more sheltered slopes remained pristine during the next few days. The reanalysis captures this overall area-average variation.
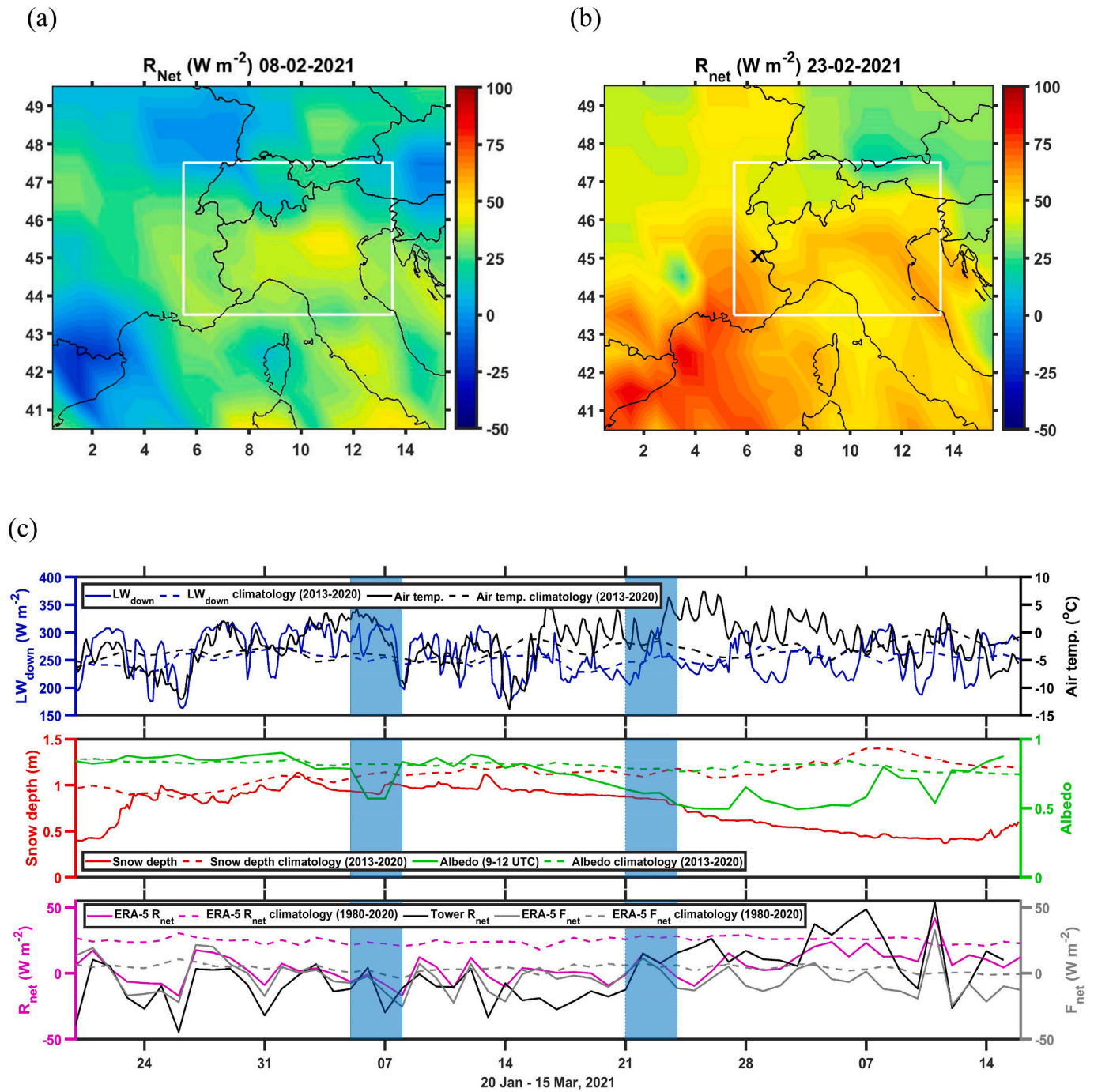
(a)

(b)

(c)

Fig. 6. Impact on albedo and snow cover at the Alps. (a)–(b) show the daily-averaged surface net radiation flux from 40.5°–49.5°N and 0°–15°E on 08 and 23 February 2021, respectively. In (c) the solid lines in the first two panels give 3-hourly downward long-wave radiation flux (W m⁻²), air temperature (°C), snow depth (m) and surface albedo from 20 January to 15 March 2021 at the FlexAlps site (cross mark in (a)), with the climatological values given by the dashed lines. The third panel is as the first two but for the surface net radiation flux (R_{net}; W m⁻²) and total energy flux (F_{net}; W m⁻²). (d) Shows R_{net} (W m⁻²) spatially-averaged values over the white box drawn in (a) from CERES and ERA-5, and F_{net} (W m⁻²) from ERA-5. In the third panel, the spatially-averaged snow depth (m) and surface albedo averaged over the grey cross points drawn in (e)–(h) are given, while the spatial maps of surface albedo at 12:30 UTC and snow depth at 00:30 UTC on 05 February 2021 and 05 March 2021 are plotted in (e)–(h).

### 2.4. Climatology and trends of ARs and severe dust storms over Europe

In the previous subsections, the focus was on the February 2021 AR events. However, given the substantial impacts the dusty ARs had on the surface fields in the Alps, most notably their contribution for the observed reduction in the snow cover, it is of interest to investigate their long-term spatio-temporal trends. In an attempt to quantify the

interrelation of their spatial extent, composite daily mean of IVT differences (kg m⁻¹ s⁻¹) between AR days and all-day climatology (1980–2017) for January–May period is shown in Fig. 7A. Similarly, composite daily mean of AOD differences between AODs on AR days and AODs on all-day climatology (1980–2017) for January–May period, is shown in Fig. 7B. These composites show that high IVT values over northwest Africa are associated with high AOD values over northern
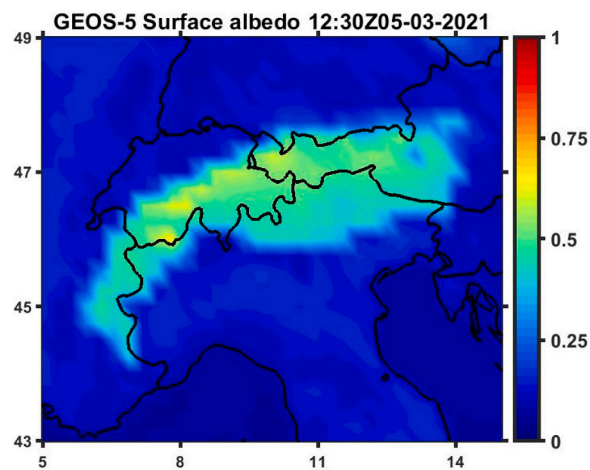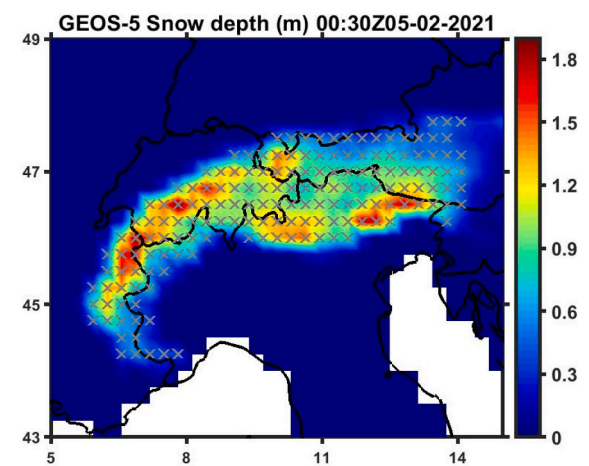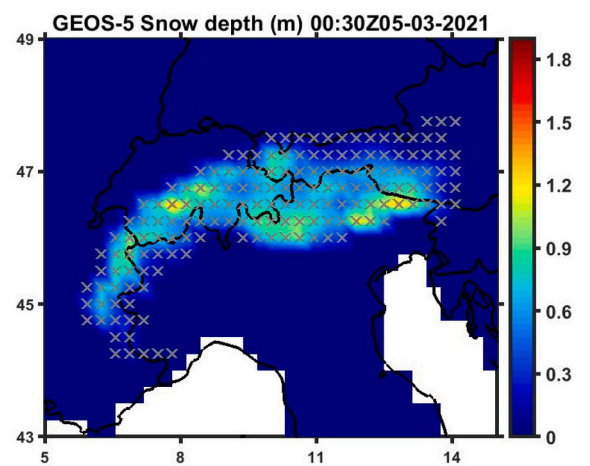
(d)
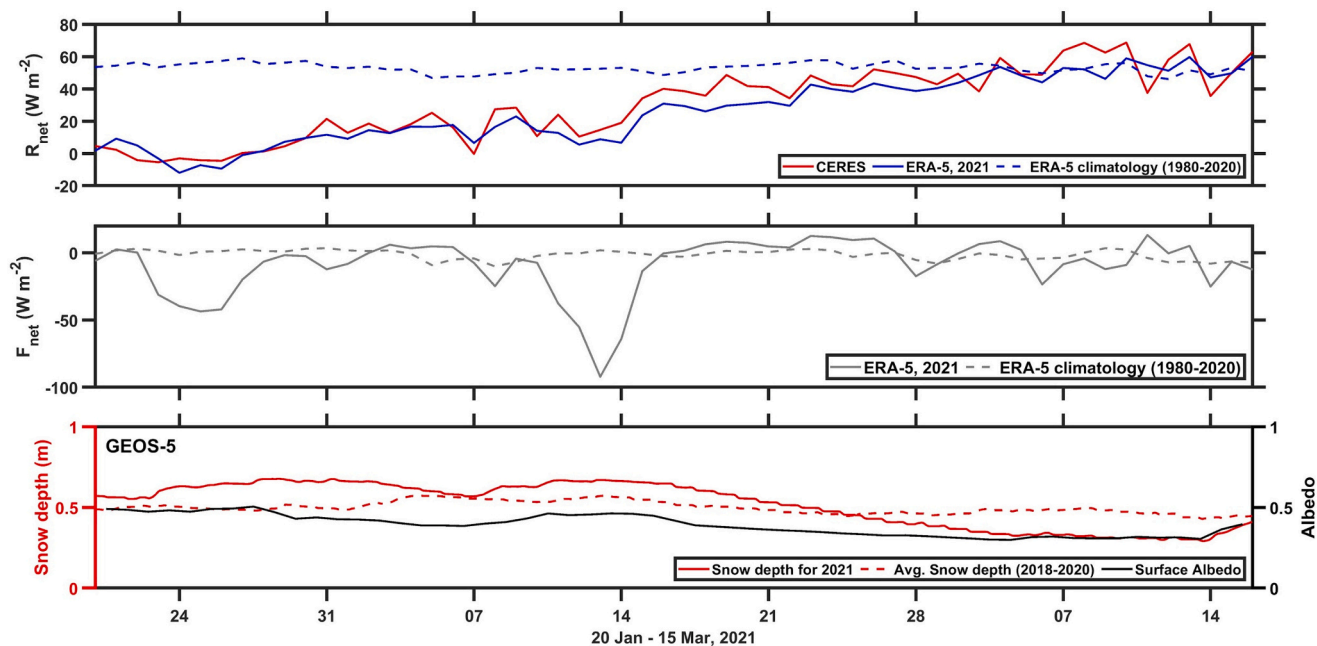
(e)
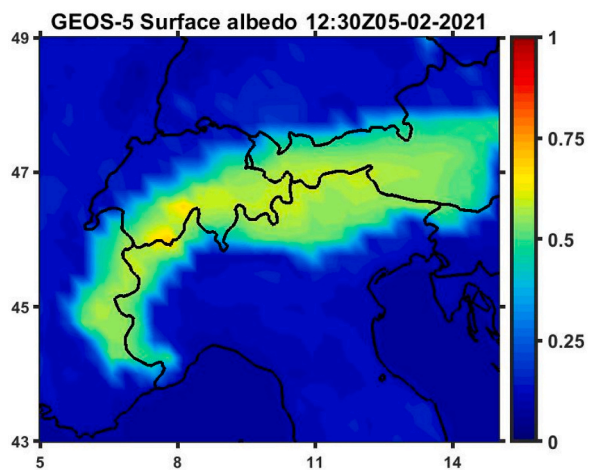
(f)

(g)

(h)

Fig. 6. (*continued*).

Sahara and southern Europe. A southwest to northeast structure in the IVT anomalies is seen, with maximum values around the Alps of 10 to 20 kg m^{-1} s^{-1}. The peak in the AOD is along the AR region with values in excess of 0.1 mostly confined to northern Africa and the Mediterranean Sea. In extreme events, such as those of February 2021, the higher IVT and AOD values can extend well into central and even northern Europe.

The yearly IVT and AOD time-series, averaged over January–May, exhibits considerable inter-annual variability (Fig. 7C), with some of the relevant modulating modes being NAO, ENSO and the AMO (Fig. 7D). ENSO is a well-known mode of variability linked to changes in the equatorial Pacific SSTs, with impacts throughout the world (e.g., Sterl et al., 2007). The NAO is related to the changes in strength of the Icelandic Low and the Azores High. In its positive phase, both centers are stronger than normal, favoring an enhanced and northward displaced storm track, while in the negative NAO phase, the Atlantic storm track is weaker and shifted to the south. ENSO and NAO events are related to each other, with El Nino episodes favoring NAO- (Toniazzo and Scaife, 2006), and La Nina events NAO+ (Hardiman et al., 2019). The maximum of AR days occurs when the NAO is in negative phase (NAO-, red curve in Fig. 7C). This is because when the NAO is negative the jet stream is displaced southward and blocking highs occur over the Atlantic favoring ARs towards North Africa and then Europe, as highlighted in Section 2 of this study. Hence, the key climate index for AR days over Europe is the NAO and more specifically its negative phase which is generally promoted by positive ENSO phase. Fig. 7E shows the correlation between maximum AR days and NAO negative phase. Other modes of variability as well as non-linear interactions between them can also influence the phase of the NAO such as the AMO which samples the variation of the North Atlantic SSTs on multidecadal time-scales (Knight et al., 2006; Nigam and Guan, 2011) and therefore modulates the NAO phase. The correlation of ARs occurrence with the NAO index is −0.65, with the ENSO index +0.26 and with the AMO index +0.39 (Fig. 7E).

Regarding the time-series of the ARs and AODs (Fig. 7C and D), it can be concluded that, for example, ARs over northwestern Africa and southwestern Europe are more common in NAO- years (e.g. late 1980s and early 1990s; 2010). This is in line with Guan and Waliser (2015), who noted that ARs occur more often over northern Europe in NAO+ episodes, and over southern Europe in NAO- events. Given the aforementioned link between ENSO and NAO, El Nino events favor the occurrence of AR events over southern Europe and northern Africa, due to the southerly displaced storm track, as also found in Guan and Waliser (2015). The warmer than average SSTs over the North Atlantic and Mediterranean Sea, together with slight westward displacement of the Icelandic Low and eastwards displacement of the Azores high and associated shift in the Atlantic storm track in AMO+ events (Borgel et al., 2020), may also increase the number of AR events, in line with the positive correlation between the two. This is also consistent with the fact that AMO+ events tend to favor NAO- states (O'Reilly et al., 2017). The western and central European area-averaged AOD is only positively correlated with the AMO index, with the +0.34 coefficient statistically significant at the 95% confidence level.

Additionally, slight increase in ARs frequency (+1 day per 30 years) can be depicted in Fig. 7C. At the same time, AODs over Europe increased by 0.01 in 30 years (statistically significant at the 95% confidence level (Fig. 7D)). However, the number of extreme dust events did not increase during the 1980–2017 period (not shown), which suggests that the intensity of the extreme dust events may have increased but not their frequency.

AR events over northwest Africa and dust events over Europe are correlated in time (Fig. 7F), with the statistics summarized in Table S1. Dust days are categorized as strong if Mean + 2 × STD ≤ AOD < Mean + 4 × STD, and extreme if AOD ≥ Mean + 4 × STD, where Mean and STD are the long-term mean and standard deviation of the AOD (Gkiaks et al., 2013). We found that, roughly 78% of the ARs coincide with the combined strong and extreme dust events, with this fraction ranging from 50 to 100% (Fig. 7F). On the other hand, only roughly 18% of strong and extreme dust events are associated with ARs. This highlights that ARs are more likely to be associated with dust events than the other way-round reflecting on the fact that dust events can be generated by other dynamical forcings such as cyclones or fronts that are not necessarily associated with an AR.

3. Summary and conclusions

In this study, the identification of dusty atmospheric rivers (ARs) stretching from the Sahara all the way to Europe is achieved for the first time using a mixture of satellite-derived and ground-based measurements and state-of-the-art reanalysis datasets. The crucial role of dusty atmospheric rivers in the reduction of snow cover over the European Alps as well as their impacts on the surface meteorological fields over Europe is then investigated during two dusty atmospheric rivers in February 2021.

The two ARs that affected Europe in February 2021 were linked with distinct atmospheric patterns. The first, from 04 to 08 February, occurred in association with a transient pattern, with a trough over the Iberian Peninsula and a ridge over southeastern Europe leading to a southerly flow in the region. The second AR, which took place from 18 to 25 February, was promoted by an omega blocking over Eastern Europe, which persisted for roughly 5 days, allowing the Saharan dust to reach Scandinavia at 60°N. This southerly-northerly aligned AR is not common in the colder months when they tend to be more zonally-oriented (Lavers and Villarini, 2013; Benedict et al., 2019). The maximum values of integrated vapour transport (IVT) associated with these ARs were in the range of 400–600 kg m^{-1} s^{-1}, i.e., more than 1.5 standard deviations above the climatological mean. The two February 2021 ARs had a similar length of about 5000 km, with a length-to-width ratio of three for the first and eight for the second, which was considerably narrower.

The dust transport associated with the ARs led to unusually high values of aerosol optical depth (AOD) over the Alps: the maximum area-averaged value of 0.85 observed on 07 February was on the higher end of the 1980–2020 climatological range, more than two standard deviations away from the mean. Daily accumulated dust loadings of up to 60 g m^{-2} were observed, one order of magnitude larger than those reported in other wintertime dust events (Varga, 2020). The anomalous AODs and associated dust mass loadings extended all the way to 80°N in the second event, owing to the persistent blocking over Europe. While mostly confined at 1–3 km above the surface, the lifted dust within the warm conveyor belt reached up to 7 km. As with the dust, the amount of moisture in the air, up to an area-averaged value of 15 kg m^{-2} of IWV, was also on the higher end of the climatological values, with normalised anomalies of up to two. This is consistent with the rather warm and moist near-surface air, with a 2-m air temperature and water vapour mixing ratio up to 8 K and 3 g kg^{-1} above average, respectively. At higher latitudes, the anomalies were even more extreme, exceeding 10 K at 80°N. The phase of the AOD and IWV time-series for February 2021 is largely similar, with the dust mixed with the moist air propagating along the AR.

Our study stress out that when ARs and dust episodes co-occur, the impact on the snow cover can be quite dramatic. At a weather station in the western Alps (the FluxAlps station), the effects of the rather moist and dusty atmosphere on the meteorological fields were quite remarkable. The snow albedo was reduced by up to 40%, the downward longwave radiation flux increased up to 50 W m^{-2} above the 1980–2020 climatology. The combined effects of albedo reduction and increased LW led to a reduction of the snow depth by up to 50 cm (or 50% of the actual value). These figures are comparable to those reported by other authors such as Skiles and Painter (2017) over the Rocky Mountains in the United States. The GEOS-5 model showed comparable changes in snow depth and albedo from early February to early March 2021 over the Alps, indicating that the measurements at the FluxAlps station were representative of those seen elsewhere in the region.

(a)

(b)

(c)

(d)

(e)

(f)
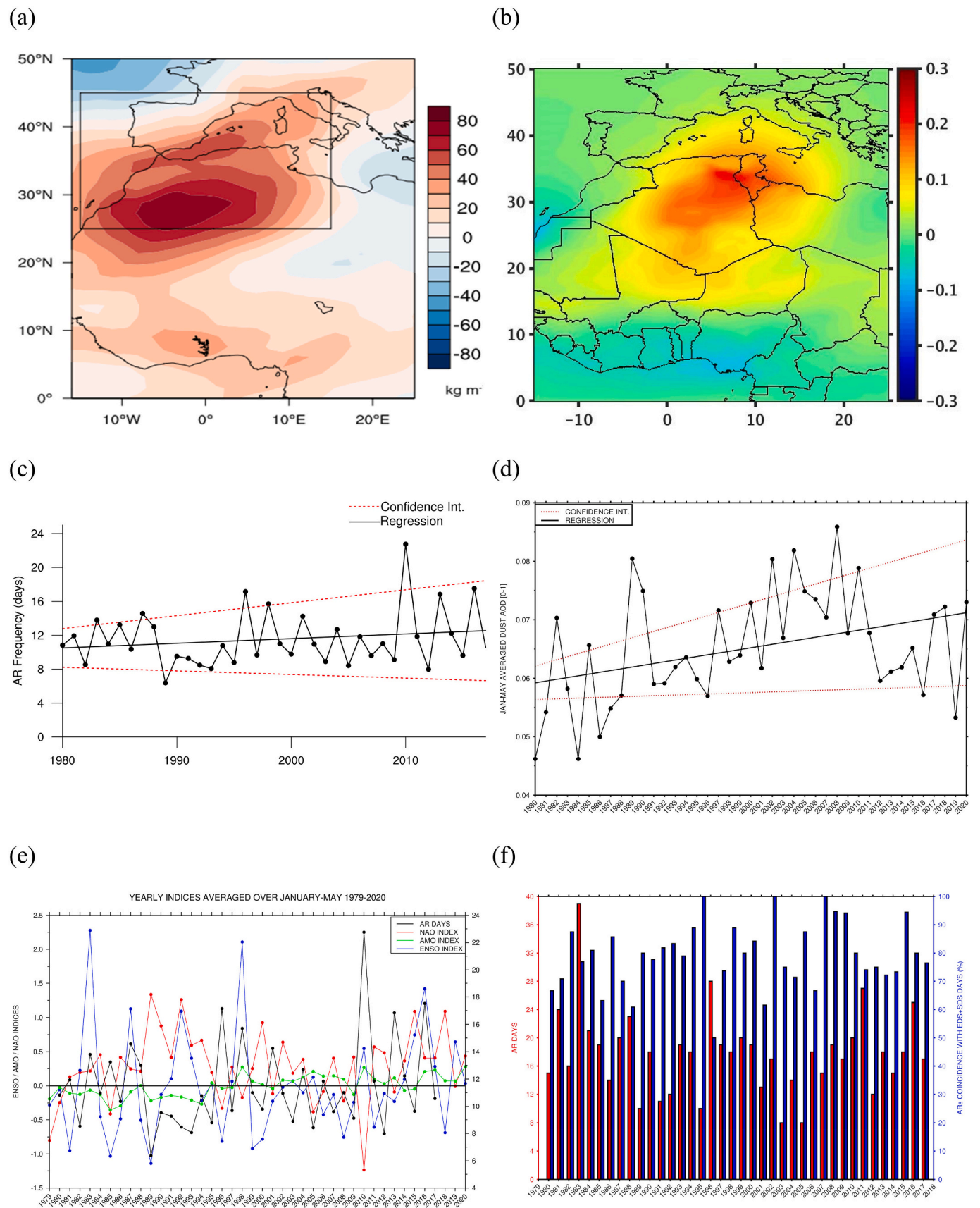
(caption on next page)

Fig. 7. Climatology and trends of ARs and Dust Events. (a) Composite daily mean IVT differences (kg m^{-1} s^{-1}) between the AR days (defined for the solid box on the map) and all-day climatology (1980–2017) for January–May period. (b) Composite daily mean dust optical depth (AOT) differences between the AR days and all-day climatology (1980–2017) for January–May period. In (c), the AR trends over 25–45°N, 15°W-15°E (black box in panel (a)) averaged over January–May of each year from 1980 to 2017 are plotted, while in (d) the trends in the dust optical depth averaged over Europe (30°-50°N, 15°W-15°E) for the same period are shown. Panel (e) gives the January–May averages of the El Nino-Southern Oscillation (ENSO; K), North Atlantic Oscillation (NAO), the Atlantic Multidecadal Oscillation (AMO; K) indices from 1979 to 2020 and the AR frequency as in (a). In panel (f), the yearly AR days (red) and the percentage of which coincided with strong dust events (SDS, Mean + 2 × STD ≤ AOD < Mean + 4 × STD) and severe dust events (SDS, AOD ≥ Mean + 4 × STD) (blue) from 1980 to 2017, are shown. The dust events are defined following Gkikas et al. (2013), with Mean and STD the climatological mean and standard deviation. (For interpretation of the references to colour in this figure legend, the reader is referred to the web version of this article.)

The effects of the ARs can also be quantified in terms of the changes in the surface net radiation flux, R_{net}, and total energy flux, F_{net}. For these fields, area-averaged anomalies of up to 250 W m^{-2}, 1 to 2 standard deviations above the climatological background, and in-situ values of up to 150 W m^{-2}, were seen during the two events. The ARs under scrutiny are large-scale features which extended over thousands of kilometers. While the focus in this study was on their impact in the Alps, the Pyrenees, a mountain range between Spain and France located in the northeastern part of the Iberian Peninsula, was also affected by the dusty ARs (Fig. 2, A, B and D, Fig. 3, fig. S1D). Hence, a comparable effect on the surface and near-surface fields, including snow cover, can be expected over the Pyrenees during these events.

In line with the climate projections of Ramos et al. (2016), Massoud et al. (2020) and Whan et al. (2020), we found a positive trend in the number of AR days over southwestern Europe and northwestern Africa in the period 1980–2017, with a typical rate of +1 day per 30 years. The dust aerosol optical depth associated with extreme dust events over Europe exhibited a positive trend as well for the same period at about +0.01 per 30 years. The positive phase of the El Nino-Southern Oscillation (ENSO), which favours the negative phase of the North Atlantic Oscillation (NAO), promotes increased ARs over western and central Europe, owing to the southerly shift in the Atlantic storm track, in line with Guan and Waliser (2015) and Zavadoff and Kirtman (2020). This is also found to be the case for the positive phase of the Atlantic Multidecadal Oscillation (AMO), which marginally favours NAO-. An El Nino and NAO+ events promote dusty episodes over Europe, in line with Moulin et al. (1997).

A statistical analysis also revealed that AR days coincide with strong to extreme dust events (statistically significant at the 95% confidence level), at an average rate of 78%, while only roughly 18% of strong and extreme dust episodes co-occur with AR events. As both are likely to be enhanced in a warming world (Ramos et al., 2016; Espinoza et al., 2018; Massoud et al., 2020; Whan et al., 2020; Payne et al., 2020), their combined effects can lead to a further reduction in the thickness and temporal and spatial extent of the snow cover over the Alps and other mountainous regions in Europe. What is more, ARs are also likely to be stronger because of the projected increase in sea surface temperatures and hence surface evaporation (Zavadoff and Kirtman, 2020). This will further exacerbate the ongoing long-term decline of roughly 8% and 5% per decade in the mean snow depth and extent of the snow cover season, respectively (Matiu et al., 2021).

While this work addresses the effects of the dusty ARs on the surface of the snowpack, in particular on the snow depth and albedo, the reported changes in the surface fluxes can also impact the internal structure of the snow layer further promoting its ablation. For example, a dusty snowpack may be more permeable with weaker capillary barriers, which may trigger the occurrence of avalanches (Baggi and Schweizer, 2009) in addition to promoting further melting. Avalanches associated with ARs have already been reported in Hatchett et al. (2017) in the western US. The melting of snow at the bottom of the pack and resulting increase in soil volumetric liquid water content is also known to foster the occurrence of snowslides (Tuzet et al., 2017, 2020; Maggioni et al., 2019). Dust radiative forcing on snow cover accounts for 70% to 83% of snow melt in the San Juan Mountains of Colorado River Basin (Painter et al., 2018).

The results of this study encourage further investigations on the effects of dust and other aerosols on snow, so as to better quantify projected changes in snow cover and their societal impacts. This including the possible role of dust deposition on the Alpine snow in the development of the 'bloody snow' phenomenon which witnessed the Alps in spring 2021. In fact, mineral dust aerosols can provide nutrients to the 'red snow' microalgae as well to other microalgae that grow on snow and ice (e.g., Nagatsuka et al., 2014). Additionally, the assessment of how well the identified atmospheric rivers are represented in current numerical models is recommended for future work in order to gain knowledge on their behavior and accurately project their trends under a warmer climate.

4. Materials and methods

The four observational datasets used in this work are listed below:

➢ Red-Green-Blue (RGB) images from the Spinning Enhanced Visible and Infrared Imager (SEVIRI; Schmetz et al., 2002) instrument on board the Meteosat Second Generation Spacecraft. These satellite images, available on a 0.05° grid every 15-min, are constructed from the 8.7, 10.8, and 12 μm brightness temperatures (Martinez et al., 2009). They allow for the identification of the dust plumes as they propagate away from the source region, as well as the clouds and moist air;

➢ Clouds and the Earth's Radiant Energy System (CERES; Wielicki et al., 1996) surface radiation fluxes. The product used is "CERES FLASH_TISA Version4" (Kratz et al., 2014), which provides daily averaged surface and Top of the Atmosphere (TOA) fluxes, and MODIS cloud properties on a 1° × 1° grid, within a week of the satellite observations;

➢ Vertical profiles of the vertical feature mask and aerosol subtype estimated from the measurements collected by the Cloud-Aerosol Lidar with Orthogonal Polarization (CALIOP) instrument, on board the Cloud-Aerosol Lidar and Infrared Pathfinder Satellite Observations (CALIPSO; Winker et al., 2003) satellite, following the algorithm detailed in Kim et al. (2018). Besides clouds, dust and polluted dust, the latter defined as the mixture of dust with biomass burning and urban pollution (Kim et al., 2018), are present over the Alps in the CALIPSO overpasses for the two AR events;

➢ In situ ground-based measurements of air temperature, relative humidity, snow depth and surface radiation and heat fluxes available on a 3-hourly basis for the FlexAlps weather station at Col du Lautaret (45.0413°N; 6.4106°E) in France. This station is located on the western side of the Alps where the effects of the ARs were clearly noticeable, and therefore is used to investigate their surface and near-surface signatures.

In addition to the observational datasets, four reanalysis products are considered in this work:

➢ ERA-5 reanalysis data (Hersbach et al., 2020), available from January 1979 up to five days behind real time, on a 0.25° × 0.25° grid and an hourly basis. This dataset is used to investigate the large-scale atmospheric conditions associated with the AR events. The 1979–2020 climatology is used to compute the anomalies and normalised anomalies.

Fields extracted from ERA-5 include the 2-meter temperature and water vapour mixing ratio, surface heat and radiative fluxes, and the integrated water vapour (IWV) and cloud liquid water content (LWC). The surface fluxes are given as mean rates over the previous hour before at a given time stamp (e.g., the fluxes at 12 UTC are the mean rates between 11 UTC and 12 UTC), and are defined as being positive if downwards into the surface. The IWV and LWC, both in units of kg m^{-2}, are defined as follows:

$$IWV = \frac{1}{g} \int_{1\,hPa}^{1000\,hPa} q dp \tag{1}$$

$$LWC = \frac{1}{g} \int_{1\,hPa}^{1000\,hPa} q_c\, dp \tag{2}$$

where g is the gravitational acceleration (9.80665 m s^{-2}), q and q_c are the water vapour and cloud liquid water mixing ratios (kg kg^{-1}), and p is the pressure, with the integrals extending from 1000 hPa to the top of the atmosphere.

➢ Global AR database available from Guan and Waliser (2019). For the climatology over 1980–2017, the AR database used is based on integrated water vapour transport (IVT; kg m^{-1} s^{-1}) derived from six-hourly ERA-Interim reanalysis (Dee et al., 2011) fields of specific humidity and vector winds at 17 pressure levels between 1000 and 300 hPa, calculated using Eq. (3) where g is the acceleration due to gravity (m s^{-2}), q is specific humidity (kg kg^{-1}), u and v are zonal and meridional winds (m s^{-1}), respectively, and dp is the pressure difference between adjacent pressure levels. For the February 2021 AR cases, the ERA5 data were used for consistency with other variables examined during those cases.

$$IVT = \sqrt{\left(\frac{1}{g} \int_{1000}^{300} qudp \right)^2 + \left(\frac{1}{g} \int_{1000}^{300} qvdp \right)^2} \tag{3}$$

The AR tracking algorithm first extracts contiguous areas of connected grid cells (objects) based on the IVT values that are above the 85th percentile but at least greater than 100 kg m^{-1} s^{-1} at each grid cell. Then, all candidate ARs are filtered so as to retain those that meet the geometrical and directional requirements such as as the direction of object-mean IVT (poleward component >50 kg m^{-1} s^{-1}), length (>2000 km), length-width ratio (>2) as detailed in Guan and Waliser (2019).

The AR frequency is expressed in units of days and was calculated independently for each grid cell by counting the number of 6-hourly time steps within AR shape boundaries and dividing by the total number of 6-hourly time steps during the analysis period. In addition, AR events (i.e., AR days) are defined as a day with at least one of the four reanalysis time steps within detected AR shape boundaries over northwest Africa and southwest Europe (25–45°N, 15°W–15°E).

➢ Modern-Era Retrospective analysis for Research and Applications version 2 (MERRA-2; Gelaro et al., 2017) reanalysis data. Given that the radiative effect of dust is one of the foci of this work, and that MERRA-2 represents aerosols and their interactions with the climate system, this dataset is also employed for analysis. MERRA-2 provides dust-related fields such as AOD and surface mass concentration at 0.625° × 0.5° spatial and 1-hour temporal resolution. The anomalies and normalised anomalies of the selected fields are extracted using the 1980–2020 climatology.

➢ Goddard Earth Observing System, Version 5 model (GEOS-5; Yasunari et al., 2011; Molod et al., 2012) forecasts. The GOddard SnoW Impurity Module (GOSWIM) snow model in GEOS-5 evaluates the deposition of dust, black carbon and organic carbon on the mass of snow by directly using the aerosol depositions from the chemical transport model (GOCART; Colarco et al., 2010) aerosol module. GEOS-5 assimilates snow depth and albedo, which makes it ideal for this study. It provides forecasts at a 0.312° × 0.25° spatial and 1-hour

temporal resolution, and is used to investigate the dusty ARs' impact on snow depth and albedo over the Alps.

The inter-annual variability in the number of AR and dust events over Europe is investigated with a focus on three modes of variability that are known to modulate them: the El Nino-Southern Oscillation (ENSO; Wang and Picaut, 2004), the North Atlantic Oscillation (NAO; Hurrell et al., 2001), and the Atlantic Multidecadal Oscillation (AMO; Enfield et al., 2001). The respective indices are defined as follows:

➢ The ENSO index is defined following Lestari and Koh (2016), based on the SST anomalies in the modified Nino3 region (4°S–4°N and 90°W–150°W) using ERA-5 data. First the index is extracted using monthly data, a 5-month running is applied to smooth out the time-series, and then the January–May yearly indices are extracted by averaging the values of the correspondent months;
➢ The NAO index is read from the National Oceanic and Atmospheric Administration (NOAA) National Centers for Environmental Information website.[1] It is generated by projecting the NAO loading pattern, defined as the first rotated empirical orthogonal function of the monthly-mean 500 hPa geopotential height anomaly over 0°–90°N, onto the daily anomalies of the 500 hPa geopotential height field over 0°–90°N (Soulard and Lin, 2017). The January–May monthly values of each year provided on the website above are used to construct the yearly time-series;
➢ The AMO index is defined based on the area-weighted average of the detrended North Atlantic sea surface temperatures (SSTs), as detailed in Enfield et al. (2001). The monthly values are downloaded from NOAA's Physical Sciences Laboratory website,[2] and are manipulated as the NAO index to generate yearly indices.

Credit author statement

Diana Francis: Conceptualization, Methodology, Investigation, Supervision, Original draft preparation and Reviewing.
Ricardo Fonseca: Formal analysis, Validation, Writing - Original draft preparation and Reviewing.
Narendra Nelli: Visualization, Data curation and Analysis.
Deniz Bozkurt: Visualization, Data curation, Analysis and Validation.
Ghislain Picard: Data curation, Analysis and Validation.
Bin Guan: Software, Data curation.

Declaration of Competing Interest

The authors declare they do not have any conflict of interest.

Acknowledgments

---

[1] https://www.ncdc.noaa.gov/teleconnections/nao/
[2] https://psl.noaa.gov/data/timeseries/AMO/

Medium-Range Weather Forecast's data portal (https://apps.ecmwf.int/datasets/). The Modern-Era Retrospective analysis for Research and Applications version 2 (MERRA-2) is available on NASA's EarthData website (https://earthdata.nasa.gov/), while the forecasts of the Goddard Earth Observing System, version 5 model (GEOS-5) are extracted from NASA's Global Modeling and Assimilation Office website (https://gmao.gsfc.nasa.gov/GEOS_systems/). The FluxAlps weather station data were obtained from Romain Biron, Institut des Geosciences de l'Environnement, France.

Appendix A. Supplementary data

Supplementary data to this article can be found online at https://doi.org/10.1016/j.atmosres.2021.105959.

References

Anghileri, D., Botter, M., Castelletti, A., Weight, H., Burlando, P., 2018. A comparative assessment of the impact of climate change and energy policies on Alpine hydropower. Water Resour. Res. 54, 9144–9161. https://doi.org/10.1029/2017WR022289.

Baggi, S., Schweizer, J., 2009. Characteristics of wet-snow avalanche activity: 20 years of observations from a high alpine valley (Dischma, Switzerland). Nat. Hazards 50, 97–108. https://doi.org/10.1007/s11069-008-9332-7.

Barkan, J., Alpert, P., 2010. Synoptic analysis of a rare event of Saharan dust reaching the Arctic region. Weather 65, 208–211. https://doi.org/10.1002/wea.503.

Barkan, J., Alpert, P., Kutiel, H., Kishcha, P., 2005. Synoptics of dust transportation days from Africa toward Italy and central Europe. J. Geophys. Res. 110, D07208. https://doi.org/10.1029/2004JD005222.

Benedict, I., Ødemark, K., Nipen, T., Moore, R., 2019. Large-Scale Flow patterns Associated with Extreme Precipitation and Atmospheric Rivers over Norway. Mon. Weather Rev. 147 (4), 1415–1428. https://doi.org/10.1175/MWR-D-18-0362.1.

Borgel, F., Frauen, C., Neumann, T., Meier, H.E.M., 2020. The Atlantic Multidecadal Oscillation controls the impact of the North Atlantic Oscillation on North European climate. Environ. Res. Lett. 15 (10), 104025 https://doi.org/10.1088/1748-9326/aba925.

Bou Karam, D., Flamant, C., Cuesta, J., Pelon, J., Williams, E., 2010. Dust emission and transport associated with a Saharan depression: February 2007 case. J. Geophys. Res. 115, D00H27 https://doi.org/10.1029/2009JD012390.

Bozkurt, D., Ezber, Y., Sen, O.L., 2019. Role of the East Asian trough on the eastern Mediterranean temperature variability in early spring and the extreme case of 2004 warm spell. Clim. Dyn. 53, 2309–2326. https://doi.org/10.1007/s00382-019-04847-5.

Bozkurt, D., Sen, O.L., Ezber, Y., Guan, B., Viale, M., Caglar, F., 2021. Influence of African atmospheric rivers on precipitation and snowmelt in the near East's highlands. J. Geophys. Res. Atmos. 126 https://doi.org/10.1029/2020JD033646 e2020JD033646.

Buehler, S.A., Ostman, S., Melsheimer, C., Holl, G., Eliasson, S., John, V.O., Blumenstock, T., Hase, F., Elgered, G., Raffalski, U., Nasuno, T., Satoh, M., Milz, M., Mendrok, J., 2012. A multi-instrument comparison of integrated water vapour measurements at a high latitude site. Atmos. Chem. Phys. 12, 10925–10943. https://doi.org/10.5194/acp-12-10925-2012.

Colaprete, A., Toon, O.B., 2003. Carbon dioxide clouds in an early dense Martian atmosphere. J. Geophys. Res. 108 (E4), 5025. https://doi.org/10.1029/2002JE001967.

Colarco, P., da Silva, A., Chin, M., Diehl, T., 2010. Online simulations of global aerosol distributions in the NASA GEOS-4 model and comparisons to satellite and ground-based aerosol optical depth. J. Geophys. Res. 115, D14207. https://doi.org/10.1029/2009JD012820.

Davolio, S., Della Fera, S., Laviola, S., Miglietta, M.M., Levizzani, V., 2020. Heavy precipitation over Italy from the Mediterranean Storm "Vaia" in October 2018: assessing the role of an atmospheric river. Mon. Weather Rev. 148, 3571–3588. https://doi.org/10.1175/MWR-D-20-0021.1.

Dee, D.P., Uppala, S.M., Simmons, A.J., Berrisford, P., Poli, P., Kobayashi, S., Andrae, U., Balmaseda, M.A., Balsamo, G., Bauer, P., Bechtold, P., Beljaars, A.C.M., van de Berg, L., Bidlot, J., Bormann, N., Delsol, C., Dragani, R., Fuentes, M., Geer, A.J., Haimberger, L., Healy, S.B., Hersbach, H., Holm, E.V., Isaksen, L., Kallberg, P., Kohler, M., Matricardi, M., McNally, A.P., Monge-Sanz, B.M., Morcrette, J.-J., Park, B.-K., Peaubey, C., de Rosnay, P., Tavolato, C., Thepaut, J.-N., Virtart, F., 2011. The ERA-Interim reanalysis: configuration and performance of the data assimilation system. Q. J. R. Meteorol. Soc. 137, 553–597. https://doi.org/10.1002/qj.828.

Dezfuli, A., 2020. Rare atmospheric river caused record floods across the Middle East. Bull. Am. Meteorol. Soc. 101 (4), E394–E400. https://doi.org/10.1175/BAMS-D-19-0247.1.

Di Mauro, B., Fava, F., Ferrero, L., Garzonio, R., Baccolo, G., Delmonte, B., Colombo, R., 2015. Mineral dust impact on snow radiative properties in the Alps combining ground, UAV, and satellite observations. J. Geophys. Res. Atmos. 120, 6080–6097. https://doi.org/10.1002/2015JD023287.

Di Mauro, B., Garzonio, R., Rossini, M., Filippa, G., Pogliotti, P., Galvagno, M., Morra di Cella, U., Migliavacca, M., Baccolo, G., Clemenza, M., Delmonte, B., Maggi, V., Dumont, M., Tuzet, F., Lafaysse, M., Morin, S., Cremonese, E., Colombo, R., 2019.

Saharan dust events in the Alps: role in snowmelt and geochemical characterization. Cryosphere 13, 1147–1165. https://doi.org/10.5194/tc-13-1147-2019.

Dumont, M., Tuzet, F., Gascoin, S., Picard, G., Kutuzov, S., Lafaysse, M., Cluzet, B., Nheili, R., Painter, T.H., 2020. Accelerated snow melt in the Russian Caucasus mountains after the Saharan dust outbreak in March 2018. J. Geophys. Res. Earth Surf. 125, e2020JF005641 https://doi.org/10.1029/2020JF005641.

Enfield, D.B., Mestas-Nunez, A.M., Trimble, P.J., 2001. The Atlantic Multidecadal Oscillation and its relationship to rainfall and river flows in the continental U.S. Geophys. Res. Lett. 28, 2077–2080. https://doi.org/10.1029/2000GL012745.

Espinoza, V., Waliser, D.E., Guan, B., Lavers, D.A., Ralph, F.M., 2018. Global analysis of climate change projection effects on atmospheric rivers. Geophys. Res. Lett. 45, 4299–4308. https://doi.org/10.1029/2017GL076968.

Evan, A., Eisenman, I., 2021. A mechanism for regional variations in snowpack melt under rising temperature. Nat. Clim. Chang. https://doi.org/10.1038/s41558-021-00996-w.

Fiedler, S., Schepanski, K., Knippertz, P., Heinold, B., Tegen, I., 2014. How important are atmospheric depressions and mobile cyclones for emitting mineral dust aerosol in North Africa? Atmos. Chem. Phys. 14, 8983–9000. https://doi.org/10.5194/acp-14-8983-2014.

Francis, D., Eayrs, C., Chaboureau, J.-P., Mote, T., Holland, D.M., 2018. Polar jet associated circulation triggered a Saharan cyclone and derived the poleward transport of the African dust generated by the cyclone. J. Geophys. Res. Atmos. 123, 11,899–11,917. https://doi.org/10.1029/2018JD029095.

Francis, D., Eayrs, C., Chaboureau, J.-P., Mote, T., Holland, D.M., 2019. A meandering polar jet caused the development of a Saharan cyclone and the transport of dust toward Greenland. Adv. Sci. Res. 16, 49–56. https://doi.org/10.5194/asr-16-49-2019.

Francis, D., Chaboureau, J.-P., Nelli, N., Cuesta, J., Alshamsi, N., Temimi, M., Xue, L., Pauluis, O., 2020a. Summertime dust storms over the Arabian Peninsula and impacts on radiation, circulation, cloud development and rain, Atmospheric Research, 2020. ISSN 105364, 0169–8095. https://doi.org/10.1016/j.atmosres.2020.105364.

Francis, D., Mattingly, K.S., Temimi, M., Massom, R., Heil, P., 2020b. On the crucial role of atmospheric rivers in the two major Weddell Polynya events in 1973 and 2017 in Antarctica. Sci. Adv. 6, eabc2695. https://advances.sciencemag.org/content/6/46/eabc2695.

Francis, D., Nelli, N., Fonseca, R., Weston, M., Flamant, C., Cherif, C., 2021. The dust load and radiative impact associated with the June 2020 historical Saharan dust storm. Atmos. Environ. 268, 118808. ISSN 1352-2310. https://doi.org/10.1016/j.atmosenv.2021.118808.

Gelaro, R., McCarty, W., Suarez, M.J., Todling, R., Molod, A., Takacs, L., Randles, C.A., Darmenov, A., Bosilovich, M.G., Reichle, R., Wargan, K., Coy, L., Cullather, R., Draper, C., Akella, S., Buchard, V., Conaty, A., da Silva, A.M., Gu, W., Kim, G.-K., Koster, R., Lucchesi, R., Merkova, D., Nielsen, J.E., Partyka, G., Pawson, S., Putman, W., Rienecker, M., Schubert, S.D., Sienkiewicz, M., Zhao, B., 2017. The modern-era retrospective analysis for research and applications, version 2 (MERRA-2). J. Clim. 30, 5419–5454. https://doi.org/10.1175/JCLI-D-16-0758.1.

Gimeno, L., Nieto, R., Vazquez, M., Lavers, D., 2014. Atmospheric Rivers: a mini-review. Front. Earth Sci. 2, 2296–6463. https://doi.org/10.3389/feart.2014.00002.

Gkikas, A., Hatzianastassiou, N., Mihalopoulos, N., Katsoulis, V., Kazadzis, S., Pey, J., Querol, X., Torres, O., 2013. The regime of intense desert dust episodes in the Mediterranean based on contemporary satellite observations and ground measurements. Atmos. Chem. Phys. 13, 12135–12154. https://doi.org/10.5194/acp-13-12135-2013.

Guan, B., Waliser, D.E., 2015. Detection of atmospheric rivers: evaluation and application of an algorithm for global studies. J. Geophys. Res. Atmos. 120, 12514–12535. https://doi.org/10.1002/2015JD024257.

Guan, B., Waliser, D.E., 2019. Tracking atmospheric rivers globally: Spatial distributions and temporal evolution of life cycle characteristics. J. Geophys. Res. Atmos. 124 (23), 12523–12552. https://doi.org/10.1029/2019JD031205.

Guan, B., Waliser, D.E., Ralph, F.M., Fetzer, E.J., Neiman, P.J., 2016. Hydrometeorological characteristics of rain-on-snow events associated with atmospheric rivers. Geophys. Res. Lett. 43, 2964–2973. https://doi.org/10.1002/2016GL067978.

Hardiman, S.C., Dunstone, N.J., Scaife, A.A., Smith, D.M., Ineson, S., Lim, J., Fereday, D., 2019. The impact of strong El Niño and La Niña events on the North Atlantic. Geophys. Res. Lett. 46, 2874–2883. https://doi.org/10.1029/2018GL081776.

Hatchett, B.J., Burak, S., Rutz, J.J., Oakley, N.S., Bair, E.H., Kaplan, M.L., 2017. Avalanche fatalities during Atmospheric river events in the Western United States. J. Hydrometeorol. 18 (5), 1359–1374.

Hegyu, B.M., Taylor, P.C., 2018. The unprecedented 2016-2017 Arctic Sea ice growth season: the crucial role of atmospheric rivers and longwave fluxes. Geophys. Res. Lett. 45, 5204–5212. https://doi.org/10.1029/2017GL076717.

Helmert, J., Heinold, B., Tegen, I., Hellmuth, O., Wendisch, M., 2007. In the direct and semidirect effects of Saharan dust over Europe: a modeling study. J. Geophys. Res. 112, D13208. https://doi.org/10.1029/2006JD007444.

Hersbach, H., Bell, B., Berrisford, P., Dahlgren, P., Horanyi, A., Munoz-Sebater, J., Nicolas, J., Radu, R., Schepers, D., Simmons, A., Soci, C., 2020. The ERA5 Global Reanalysis: achieving a detailed record of the climate and weather for the past 70 years. In: European Geophysical Union General Assembly 2020, May 3–8, Vienna, Austria. https://doi.org/10.5194/egusphere-egu2020-10375.

Hurrell, J.W., Kushnir, Y., Visbeck, M., 2001. The North Atlantic Oscillation. Science 291 (5504), 603–605. https://doi.org/10.1126/science.1058761.

Ionita, M., Nagavciuc, V., Guan, B., 2020. Rivers in the sky, flooding on the ground: the role of atmospheric rivers in inland flooding in central Europe. Hydrol. Earth Syst. Sci. 24, 5125–5147. https://doi.org/10.5194/hess-24-5125-2020.

Israelevich, P., Ganor, E., Alpert, P., Kishcha, P., Stupp, A., 2012. Predominant transport paths of Saharan dust over the Mediterranean Sea to Europe. J. Geophys. Res. 117, D02205. https://doi.org/10.1029/2011JD016482.

Karydis, V.A., Kumar, P., Barahona, D., Sokolik, I.N., Nenes, A., 2011. On the effect of dust particles on global cloud condensation nuclei and cloud droplet number. J. Geophys. Res. 116, D23204. https://doi.org/10.1029/2011JD016283.

Kaskaoutis, D.G., Rashki, A., Dumka, U.C., Mofidi, A., Kambezidis, H.D., Psiloglou, B.E., Karagiannis, D., Petrinoli, K., Gavriil, A., 2019. Atmospheric dynamics associated with exceptionally dusty conditions over the eastern Mediterranean and Greece in March 2018. Atmos. Res. 218, 269–284. https://doi.org/10.1016/j.atmosres.2018.12.009.

Kim, M.-H., Omar, A.H., Tackett, J.L., Vaughan, M.A., Winker, D.M., Trepte, C.R., Hu, Y., Liu, Z., Poole, L.R., Pitts, M.C., Kar, J., Magill, B.E., 2018. The CALIPSO version 4 automated aerosol classification and lidar ratio selection algorithm. Atmos. Meas. Tech. 11, 6107–6135. https://doi.org/10.5194/amt-11-6107-2018.

Kingston, D.G., Lavers, D.A., Hannah, D.M., 2016. Floods in the Southern Alps of New Zealand: the importance of atmospheric rivers. Hydrol. Process. 30, 5063–5070. https://doi.org/10.1002/hyp.10982.

Knight, J.R., Folland, C.K., Scaife, A.A., 2006. Climate impacts of the Atlantic Multidecadal Oscillation. Geophys. Res. Lett. 33, L17706. https://doi.org/10.1029/2006GL026242.

Kratz, D.P., Stackhouse, P.W., Gupta, S.K., Wilber, A.C., Sawaengphokhai, P., McGarragh, G.R., 2014. The fast longwave and shortwave flux (FLASHFlux) data product: Single-scanner footprint fluxes. J. Appl. Meteorol. Climatol. 53 (4), 1059–1079. https://doi.org/10.1175/JAMC-D-13-061.

Lavers, D.A., Villarini, G., 2013. The nexus between atmospheric rivers and extreme precipitation across Europe. Geophys. Res. Lett. 40, 3259–3264. https://doi.org/10.1002/grl.50636.

Lestari, R.K., Koh, T.-Y., 2016. Statistical evidence for asymmetry in ENSO-IOD Interactions. Atmosphere-Ocean 54 (5), 498–504. https://doi.org/10.1080/070559900.2016.1211084.

Little, K., Kingston, D.G., Cullen, N.J., Gibson, P.B., 2019. The role of atmospheric Rivers for extreme ablation and snowfall events in the Southern Alps of New Zealand. Geophys. Res. Lett. 46, 2761–2771. https://doi.org/10.1029/2018GL081669.

Maggioni, M., Godone, D., Frigo, B., Freppaz, M., 2019. Snow gliding and glide-snow avalanches: recent outcomes from two experimental test sites in Aosta Valley (northwestern Italian Alps). Nat. Hazards Earth Syst. Sci. 19, 2667–2676. https://doi.org/10.5194/nhess-19-2667-2019.

Martinez, M.A., Ruiz, J., Cuevas, E., 2009. Use of SEVIRI images and derived products in a WMO sand and dust storm warning system. IOP Conf. Ser. Earth Environ. Sci. 7, 012004 https://doi.org/10.1088/1755-1307/7/1/012004.

Massoud, E., Massoud, T., Guan, B., Sengupta, A., Espinoza, V., De Luna, M., Raymond, C., Waliser, D., 2020. Atmospheric rivers and precipitation in the Middle East and North Africa (MENA). Water 12, 2863. https://doi.org/10.3990/w12102863.

Matiu, M., Crespi, A., Bertoldi, G., Carmagnola, C.M., Marty, C., Morin, S., Schöner, W., Cat Berro, D., Chiogna, G., De Gregorio, L., Kotlarski, S., Majone, B., Resch, G., Terzago, S., Valt, M., Beozzo, W., Cianfarra, P., Gouttevin, I., Marcolini, G., Notarnicola, C., Petitta, M., Scherrer, S.C., Strasser, U., Winkler, M., Zebisch, M., Cicogna, A., Cremonini, R., Debernardi, A., Faletto, M., Gaddo, M., Giovannini, L., Mercalli, L., Soubeyroux, J.-M., Sušnik, A., Trenti, A., Urbani, S., Weilguni, V., 2021. Observed snow depth trends in the European Alps: 1971 to 2019. Cryosphere 15, 1343–1382. https://doi.org/10.5194/tc-15-1343-2021.

Molod, A., Takacs, L., Suarez, M., Bacmeister, J., Song, I.-S., Eichmann, A., 2012. The GEOS-5 Atmospheric General Circulation Model: mean climate and Development from MERRA to Fortuna. In: Technical Report Series on Global Modeling and Data Assimilation, vol. 28. Available online at: https://gmao.gsfc.nasa.gov/pubs/docs/tm28.pdf.

Mott, R., Vionnet, V., Grünewald, T., 2018. The seasonal snow cover dynamics: review on wind-driven coupling processes. Front. Earth Sci. 6, 197. https://doi.org/10.3389/feart.2018.00197.

Moulin, C., Lambert, C., Dulac, F., Dayan, U., 1997. Control of atmospheric export of dust from North Africa by the North Atlantic Oscillation. Nature 387, 691–694. https://doi.org/10.1038/42679.

Nagatsuka, N., Takeuchi, N., Uetake, J., Shmida, R., 2014. Mineralogical composition of cryoconite on glaciers in northwest Greenland. Bull. Glaciol. Res. 32, 107–114. Released September 26, 2014, Online ISSN 1884-8044, Print ISSN 1345-3807. https://doi.org/10.5331/bgr.32.107.

Nigam, S., Guan, B., 2011. Atlantic tropical cyclones in the twentieth century: natural variability and secular change in cyclone count. Clim. Dyn. 36, 2279–2293. https://doi.org/10.1007/s00382-010-0908-x.

O'Reilly, Christopher H., Woollings, T., Zannam, L., 2017. The dynamical influence of the atlantic multidecadal oscillation on continental climate. J. Clim. 30 (18), 7213–7230. https://doi.org/10.1175/JCLI-D-16-0345.1.

Painter, T.H., Skiles, S.M., Deems, J.S., Brandt, W.T., Dozier, J., 2018. Variation in rising limb of Colorado River snowmelt runoff hydrograph controlled by dust radiative forcing in snow. Geophys. Res. Lett. 45, 797–808. https://doi.org/10.1002/2017GL075826.

Pasquier, J.T., Pfahl, S., Grams, C.M., 2019. Modulation of atmospheric river occurrence and associated precipitation extremes in the North Atlantic Region by European weather regimes. Geophys. Res. Lett. 46, 1014–1023. https://doi.org/10.1029/2018GL081194.

Payne, A.E., Demory, M.E., Leung, L.R., et al., 2020. Responses and impacts of atmospheric rivers to climate change. Nat. Rev. Earth Environ. 1, 143–157. https://doi.org/10.1038/s43017-020-0030-5.

Ralph, F.M., Dettinger, M., Lavers, D., Gorodetskaya, I.V., Martin, A., Viale, M., White, A. B., Oakley, N., Rutz, J., Spackman, J.R., Wernli, H., Cordeira, J., 2017. Atmospheric rivers emerge as a global science and applications focus. Bull. Am. Meteorol. Soc. 98, 1969–1973. https://doi.org/10.1175/BAMS-D-16-0262.1.

Ralph, F.M., Rutz, J.J., Cordeira, J.M., Dettinger, M., Anderson, M., Reynolds, D., Schick, L.J., Smallcomb, C., 2019. A scale to characterize the strength and impacts of atmospheric rivers. Bull. Am. Meteorol. Soc. 100 (2), 269–289. https://doi.org/10.1175/BAMS-D-18-0023.1.

Ramos, A.M., Tomé, R., Trigo, R.M., Liberato, M.L.R., Pinto, J.G., 2016. Projected changes in atmospheric rivers affecting Europe in CMIP5 models. Geophys. Res. Lett. 43, 9315–9323. https://doi.org/10.1002/2016GL070634.

Rixen, C., Twitch, M., Lardelli, C., Gallati, D., Pohl, M., Putz, M., Bebi, P., 2011. Winter tourism and climate change in the alps: an assessment of resource consumption, snow reliability, and future snowmaking potential. Mt. Res. Dev. 31, 229–236. https://doi.org/10.1659/MRD-JOURNAL-D-10-00112.1.

Rodriguez, E., Frioud, M., Gausa, M., Stebel, K., Mogo, S., Prats, N., Torres, B., Toledano, C., Bastidas, A., Berjon, A., Cachorro, V., de Frutos, A.M., 2008. Optical properties of tropospheric aerosols derived from lidar and sun photometer measurements at ALOMAR (69N) in 2005 and 2006. Opt. Pura y Aplicada 41 (2), 183–190. Available online at: https://www.sedoptica.es/Menu_Volumenes/Pdfs/296.pdf.

Schmetz, J., Pili, P., Tjemkes, S., Just, D., Kerkmann, J., Rota, S., Ratier, A., 2002. An introduction to Meteosat Second Generation (MSG). Bull. Am. Meteorol. Soc. 83, 977–992. https://doi.org/10.1175/1520-0477(2002)083,0977:AITMSG.2.3.CO;2.

Shinoda, T., Zamudio, L., Guo, Y., Metzger, E.J., Fairall, C.W., 2019. Ocean variability and air-sea fluxes produced by atmospheric rivers. Sci. Rep. 9, 2152. https://doi.org/10.1038/s41598-019-38562-2.

Skiles, S., Painter, T., 2017. Daily evolution of in dust and black carbon content, snow grain size, and snow albedo during snowmelt, Rocky Mountains, Colorado. J. Glaciol. 63 (237), 118–132. https://doi.org/10.1017/jog.2016.125.

Soulard, N., Lin, H., 2017. The spring relationship between the Pacific-North American pattern and the North Atlantic Oscillation. Clim. Dyn. 48, 619–629. https://doi.org/10.1007/s00382-016-3098-3.

Sterl, A., van Oldenborgh, G.J., Hazeleger, W., Burgers, G., 2007. On the robustness of ENSO teleconnections. Clim. Dyn. 29, 469–485. https://doi.org/10.1007/s00382-007-0251-z.

Stibal, M., Box, J.E., Cameron, K.A., Langen, P.L., Yallop, M.L., Mottram, R.H., Ahlstrøm, A.P., 2017. Algae drive enhanced darkening of bare ice on the Greenland ice sheet. Geophys. Res. Lett. 44, 11,463–11,471. https://doi.org/10.1002/2017GL075958.

Tedesco, M., Doherty, S., Fettweis, X., Alexander, P., Jeyaratnam, J., Stroeve, J., 2016. The darkening of the Greenland ice sheet: trends, drivers, and projections (1981–2100). Cryosphere 10 (2), 477–496. https://doi.org/10.5194/tc-10-477-2016.

Theurillat, J.-P., Guisan, A., 2001. Potential impact of climate change on vegetation in the alps: a review. Clim. Chang. 50, 77–109. https://doi.org/10.1023/A:1010632015572.

Thomas, M.A., Devasthale, A., Tjernström, M., Ekman, A.M.L., 2019. The relation between aerosol vertical distribution and temperature inversions in the Arctic in winter and spring. Geophys. Res. Lett. 46, 2836–2845. https://doi.org/10.1029/2018GL081624.

Toniazzo, T., Scaife, A., 2006. The influence of ENSO on winter North Atlantic climate. Geophys. Res. Lett. 33, L24704. https://doi.org/10.1029/2006GL027881.

Tuzet, F., Dumont, M., Lafaysse, M., Picard, G., Arnaud, L., Voisin, D., Lejeune, Y., Charrois, L., Nabat, P., Samuel, M., 2017. A multi-layer physically-based snowpack model simulating direct and indirect radiative impacts of light-absorbing impurities in snow. Cryosphere 11, 2633–2653. https://doi.org/10.5194/tc-11-2633-2017.

Tuzet, F., Dumont, M., Picard, G., Lamare, M., Voisin, D., Lafaysse, M., Larue, F., Revuelto, J., Arnaud, L., 2020. Quantification of the radiative impact of light-absorbing particles during two contrasted snow seasons at Col du Lautaret (2058 m a.s.l., French Alps). Cryosphere 14, 4553–4579. https://doi.org/10.5194/tc-14-4553-2020.

Varga, G., 2020. Changing nature of Saharan dust deposition in the Carpathian Basin (Central Europe): 40 years of identified North African dust events (1979-2018). Environ. Int. 139, 105712 https://doi.org/10.1016/j.envint.2020.105712.

Voss, K., 2020. What Makes an Atmospheric River Dusty? Spatio-temporal Characteristics and Drivers of Dust in the Vicinity of Atmospheric Rivers along the U. S. West Coast. UC San Diego. ProQuest ID: Voss_ucsd_0033D_19344. Merritt ID: ark:/13030/m5n06fqb. Retrieved from: https://escholarship.org/uc/item/30m5n5b0.

Waliser, D., Guan, B., 2017. Extreme winds and precipitation during landfall of atmospheric rivers. Nat. Geosci. 10, 179–183. https://doi.org/10.1038/ngeo2894.

Wang, C., Picaut, J., 2004. Understanding Enso physics—a review. In: Wang, C., Xie, S., Carton, J. (Eds.), Earth's Climate. https://doi.org/10.1029/147GM02.

Whan, K., Sillmann, J., Schaller, N., Haarsma, R., 2020. Future changes in atmospheric rivers and extreme precipitation in Norway. Clim. Dyn. 54, 2071–2084. https://doi.org/10.1007/s00382-019-05099-z.

Wielicki, B.A., Barkstrom, B.R., Harrison, E.F., Lee III, R.B., Smith, G.L., Cooper, J.E., 1996. Clouds and the Earth's Radiant Energy System (CERES). An Earth observing system experiment. Bull. Am. Meteorol. Soc. 77, 853–868. https://doi.org/10.1175/1520-0477(1996)077<0853:CATERE>2.0.CO.

Wille, J.D., Favier, V., Dufour, A., Gorodetskaya, I.V., Turner, J., Agosta, C., Codron, F., 2019. West Antarctic surface melt triggered by atmospheric rivers. Nat. Geosci. 12, 911–916. https://doi.org/10.1038/s41561-019-0460-1.

Winker, D.M., Pelon, J.R., McCormick, M.P., 2003. The CALIPSO mission: Spaceborne lidar for observation of aerosols and clouds. In: Proceedings Volume 4893, Lidar

Remote Sensing 490 for Industry and Environment Monitoring III. https://doi.org/10.1117/12.466539.

Yasunari, T.J., Koster, R.D., Lau, K.-M., Aoki, T., Sud, Y.C., Yamazaki, T., Motoyoshi, H., Kodama, Y., 2011. Influence of dust and black carbon on the snow albedo in the NASA Goddard observing System version 5 land surface model. J. Geophys. Res. 116, D02210. https://doi.org/10.1029/2010JD014861.

Zavadoff, B.L., Kirtman, B.P., 2020. Dynamic and thermodynamic modulators of European atmospheric rivers. J. Clim. 33 (10), 4167–4185. https://doi.org/10.1175/JCLI-D-19-0601.1.

Zhu, Y., Newell, R.E., 1994. Atmospheric rivers and bombs. Geophys. Res. Lett. 21, 1999–2002. https://doi.org/10.1029/94GL01710.